Wave-current interaction in Willapa Bay

Maitane Olabarrieta,[1] John C. Warner,[1] and Nirnimesh Kumar[2]

[1]   This paper describes the importance of wave-current interaction in an inlet-estuary system. The three-dimensional, fully coupled, Coupled Ocean-Atmosphere-Wave-Sediment Transport (COAWST) modeling system was applied in Willapa Bay (Washington State) from 22 to 29 October 1998 that included a large storm event. To represent the interaction between waves and currents, the vortex-force method was used. Model results were compared with water elevations, currents, and wave measurements obtained by the U.S. Army Corp of Engineers. In general, a good agreement between field data and computed results was achieved, although some discrepancies were also observed in regard to wave peak directions in the most upstream station. Several numerical experiments that considered different forcing terms were run in order to identify the effects of each wind, tide, and wave-current interaction process. Comparison of the horizontal momentum balances results identified that wave-breaking-induced acceleration is one of the leading terms in the inlet area. The enhancement of the apparent bed roughness caused by waves also affected the values and distribution of the bottom shear stress. The pressure gradient showed significant changes with respect to the pure tidal case. During storm conditions the momentum balance in the inlet shares the characteristics of tidal-dominated and wave-dominated surf zone environments. The changes in the momentum balance caused by waves were manifested both in water level and current variations. The most relevant effect on hydrodynamics was a wave-induced setup in the inner part of the estuary.

Citation: Olabarrieta, M., J. C. Warner, and N. Kumar (2011), Wave-current interaction in Willapa Bay, *J. Geophys. Res.*, *116*, C12014, doi:10.1029/2011JC007387.

1.   Introduction

[2]   It is well known that the hydrodynamics and the morphological configuration of estuaries strongly depend on the following three processes: tidal wave propagation, exterior wave climate, and river discharges. Depending on the relative energy of each one, an estuary can exhibit a wave-dominant morphology, a tidal-dominant configuration, or a river-dominant one [*Dalrymple et al.*, 1992]. This is also reflected in the hydrodynamics, which has a direct effect on many parameters relevant from the ecological and biological points of view. However, the coexistence of waves, intense tidal currents, and river discharges, interacting with large amounts of sand deposits, makes these coastal systems and especially the inlets highly dynamic and complex, so that the interplay of the physical processes and the resulting dynamics are still not fully understood.

[3]   The hydrodynamic effect of different physical processes on a given coastal environment can be analyzed by using numerical models. In the specific case of inlets, wave-current combined flows can be investigated with fully coupled wave-current models. Most of the applications of these kind of models [*Liu and Dalrymple*, 1979; *Nishimura*, 1982; *Haas et al.*, 1998; *Park and Borthwick*, 2001; *Ruessink et al.*, 2001; *Perlin and Kit*, 2002; *Özkan-Haller and Li*, 2003; *Reniers et al.*, 2004; *Long and Özkan-Haller*, 2005] were focused on the analysis of surf zone dynamics and were based on depth integrated hydrodynamic models. However, in the last years different quasi-three-dimensional and three-dimensional (3-D) wave-current coupled models [*Svendsen and Putrevu*, 1994; *Putrevu and Svendsen*, 1999; *Van Dongeren et al.*, 1999; *Newberger and Allen*, 2007; *Haas and Warner*, 2009; *Uchiyama et al.*, 2010; *Weir et al.*, 2011] have been developed, but their application to field situations is still limited.

[4]   In contrast to studies of the surf zone, there are few studies focused on wave-current interaction effects in tidal inlets. In most of these cases the effects of waves on currents and the effect of tides on the wavefield were analyzed separately. *Gonzales et al.* [1985] showed, from a case study of wave-current interaction at the Columbia River entrance, that the offshore wave energy can propagate toward the river entrance, interacting with the current. They also observed that the wave height in the inlet decreases during the flood (following the current) and increases dramatically during the ebb (opposing current). The opposing current retards the

---

[1]Woods Hole Coastal and Marine Science Center, U.S. Geological Survey, Woods Hole, Massachusetts, USA.
[2]Department of Earth and Ocean Sciences, University of South Carolina, Columbia, South Carolina, USA.

advance of a wave, and a following current enhances the advance of a wave. Under the opposing current case, the wave energy transport can be completely blocked when the upstream component of the wave group velocity matches an equal current velocity. Because of the water depth variations in the entrance of inlets, waves can break, transferring their energy to wave-driven currents and turbulence. *Smith et al.* [2000] applied the wave transformation STWAVE steady state model to calculate wave heights and directions at the entrance to Willapa Bay (Washington State). The model was driven with observations from a wave buoy, and the results were compared with nearshore pressure gauge measurements. Water levels and currents in the inlet were predicted with the ADCIRC model. Results demonstrated that the dominant transformation process for waves in the bay was waves breaking over Willapa bar, and therefore the energy dissipation was controlled by the tide elevation over the bar. They concluded that the effect of currents on waves was significant only in the outer Willapa entrance channel, where currents reached 2 m/s. Wave heights on the ebb increased up to 80% and on the flood decreased up to 20%. *Smith and Smith* [2001] analyzed the wave propagation at the Ponce de Leon inlet (Florida) during two storm events, using field measurements and the STWAVE steady state model. Water levels and currents in the inlet were predicted with ADCIRC. They observed that model simulations agreed well with measurements except when incident waves were strongly nonlinear. They also observed that at this specific site wave-current interaction had a small influence compared with the refraction by changing water depth. *Kang and Di Iorio* [2006], using field measurements, analyzed depth- and current-induced effects on wave propagation into the Altamaha River Estuary using a suite of numerical runs with the STWAVE model. They observed that the ebb shoal region plays an important role in wave propagation to the inner part of the estuary. They stated that the shoal induces depth-limited breaking and that this effect dominated over current-induced breaking in the inlet. As a consequence, a tidal modulation of the wave height was observed in the inner part of the estuary.

[5] *Bertin et al.* [2009] applied the MORSYS2D morphodynamic modeling system in the wave-dominated Óbidos Inlet to understand the mechanism responsible for its dynamics. Because of the successful simulation of the observed morphological changes of the inlet, the authors concluded that in that specific site the 3-D processes, like undertows, were not significant. Through a model-based analysis, they outlined that the observed inlet infilling during maritime winters was the consequence of three main processes: the onshore component of the radiation stress gradients, acceleration and convergence of longshore transport toward the inlet, and the increase of the mean sea level inside the lagoon. *Robin et al.* [2009] analyzed the relative importance of different hydrodynamic processes on ebb-tidal delta bar migration in a very high tidal range environment, using detailed morphological and hydrodynamic measurements. Their study suggested that sediment transport and the bar morphology were induced mainly by surf processes and their associated currents. They also concluded that during high surf conditions mean flows were directed onshore, with an absence of a bed return flow. *Malhadas et al.* [2009] ana-

lyzed the effect of waves on the sea levels of Óbidos Inlet, identifying that a relevant superelevation on the lagoon sea level occurs during storm wave periods. They concluded that the superelevation depends not only on wave-induced radiations stresses that are due to waves, but also on the tidal inlet morphology (mainly depth and length).

[6] However, the relevance of the different wave-current interaction processes in the inlet zone and in the inner part of the estuary requires additional studies. In order to increase our understanding of the hydrodynamic processes in inlet-estuary systems, the main goal of the present study is to analyze the relative importance of the different wave-current interaction processes occurring in a mesotidal inlet subjected to energetic wave conditions. For that purpose a three-dimensional, fully coupled wave and current model presented by N. Kumar et al. (Implementation and applications of a vortex force formulation into a 3D ocean model, submitted to *Ocean Modelling*, 2011) is applied in Willapa Bay. Several hydrodynamic studies have been performed within this estuary. The Army Corps of Engineers carried out a field campaign during 1998–1999 in which different hydrodynamic parameters such as waves, tidal elevations, and current intensities in the inlet zone and inside the estuary were measured [*Kraus*, 2000a, 2000b]. *Smith et al.* [2000] applied the STWAVE model with tidal elevations and currents provided by the two-dimensional (2-D) version of ADCIRC to simulate waves in the inlet. *Banas and Hickey* [2005], applying the General Estuarine Ocean Model (GETM) numerical model, analyzed the residence times and water exchanges in Willapa Bay. In this study the tidal wave propagation along the estuary, interacting with different river input conditions was analyzed. *Lesser* [2009] applied the Delft3D wave-current fully coupled numerical model and analyzed the morphological evolution and the sediment transport processes in the entrance of Willapa Bay. *Lesser* [2009] used the fully coupled three-dimensional DELFT3D-SWAN numerical model to simulate the morphohydrodynamics in Willapa Bay. However, the study was more focused on sediment transport and on mid-long-term morphological processes, rather than on the effects caused by the wave-current interaction.

[7] *Uchiyama et al.* [2010] implemented the vortex-force formalism for the interaction of surface gravity waves and currents in the Regional Ocean Modeling System (ROMS). The implemented Eulerian wave-average current equations were based on the asymptotic theory by *McWilliams et al.* [2004]. The hydrodynamic model was coupled to a WKB wave-refraction model and applied successfully to the nearshore surf zone during the DUCK94 field measurement campaign. Kumar et al. (submitted manuscript, 2011) implemented the same formalism following Uchiyama's methodology into the ROMS module of the Coupled Ocean-Atmosphere-Wave-Sediment (COAWST) modeling system [*Warner et al.*, 2010]. Neither this modeling system nor the vortex-force method has been tested in tidal inlets. Therefore, the main objectives of the present study are to evaluate the model's performance in an inlet-estuary system and to analyze how the processes related to wave-current interactions affect wave dynamics and the hydrodynamics. To achieve these goals the model is evaluated making use of wave-current measurements carried out by the U.S. Army Corps
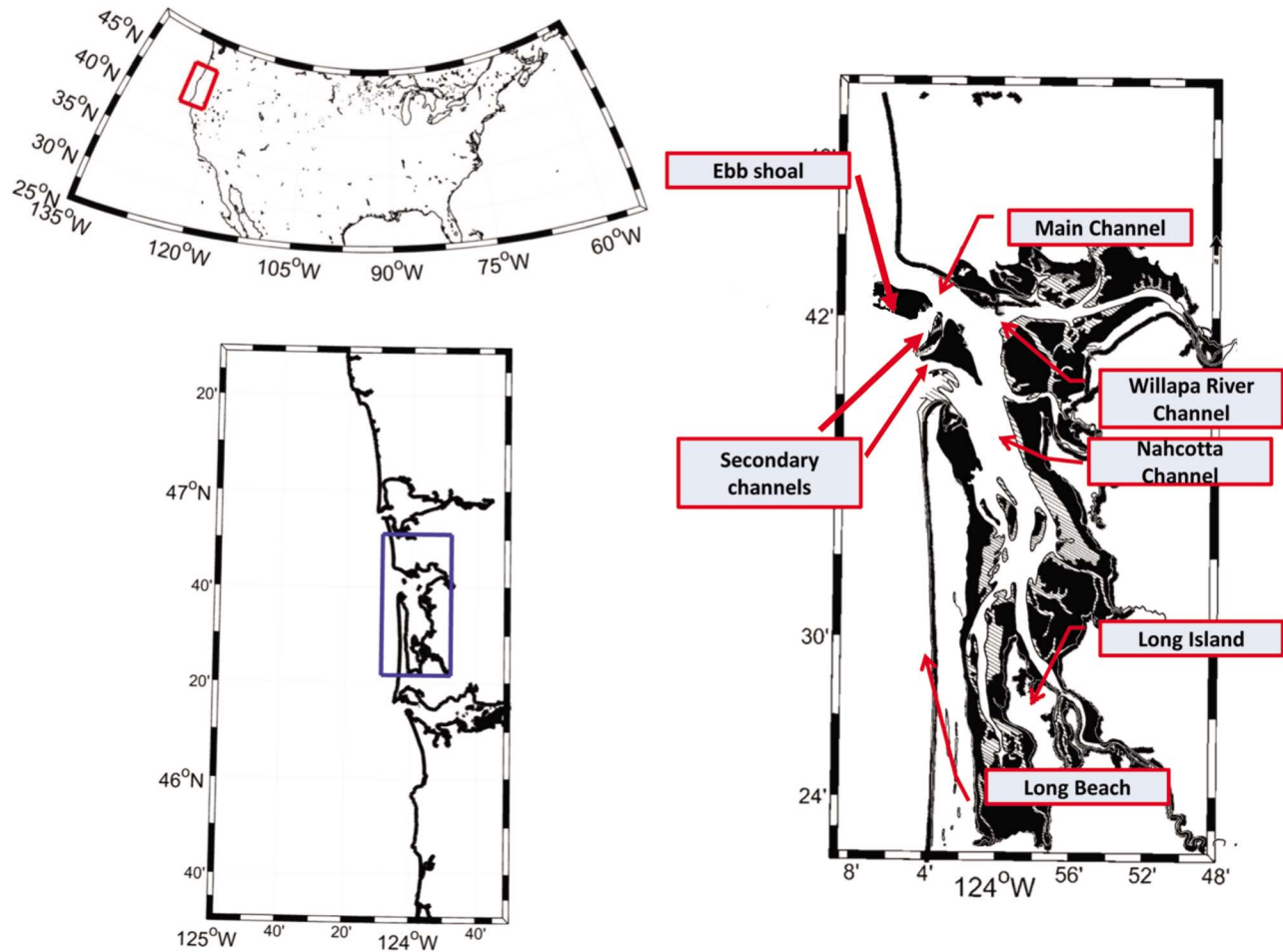
Figure 1. Location and configuration of Willapa Bay, Washington.

of Engineers. Once the model is evaluated, the contributions of different terms affecting wave-current interaction are analyzed.

[8] This paper includes six sections following this introduction. Section 2 describes Willapa Bay. Section 3 describes the ROMS-SWAN modeling system. Section 4 describes the model setup in Willapa Bay. Section 5 shows the comparison of the fully coupled model results with measured data. Section 6 is dedicated to analyze the importance of wave-current interaction in the inlet and in the inner part of the estuary. Finally, section 7 briefly summarizes the major findings of the present study.

2. The Study Zone: Willapa Bay

[9] Willapa Bay (Figure 1), located in Washington State, is the largest in a series of shallow coastal plain estuaries that spans the U.S. Pacific Northwest coast from central Washington to northern California. It is forced by strong tides (2–3 m range) and has relatively deep and unchannelized intertidal zones [*Emmett et al.*, 2000].

[10] Half of Willapa's area and volume are intertidal. The tidal prism of this estuary is approximately 8×10^8 m^3

[*Lesser*, 2009] and the inlet width is about 8 km [*Jarret*, 1976]. Willapa Bay encompasses about 260 km^2 at mean high water behind a long barrier spit to the north of the Columbia River [*Sayce*, 1976]. The main channel of the bay is oriented due north and south and is about 40 km long with a maximum width of about 10 km in midbay above Long Island. To the north is a short eastward arm at the mouth of Willapa River. Channel depths in the main channel range from 9 to 15 m with maximum depths of about 23 to 24 m below mean low water (MLW). The depths and directions of these channels indicate that they are primarily related to tidal action while the contribution of stream runoff is secondary [*Hedgpeth and Obrebski*, 1981]. In the inlet area three different channels can usually be identified. The most northern one is the deepest and is the main channel of the inlet. The other two channels are located in the middle and south part of the inlet. A very dynamic and constantly changing shallow ebb shoal is located offshore of these channels, with a mean water depth of approximately 3 m below the MLW.

[11] As explained by *Banas and Hickey* [2005], the river input occurs mostly in winter. The characteristic river flows are about 1000 m^3/s during storm winter conditions, 100 m^3/s during spring, and approximately zero during summer. The

dominant waves in this region are typically from the WNW and WSW. The mean significant wave height is about 2 m, and the mean peak period is 10 s. Although less probable than WNW waves, WSW waves can be very energetic during the winter storms. Wave heights up to 9 m, typically from the WSW to SW, can be observed in the study region during winter storms.

3. The Model

[12] In the present study the COAWST modeling system [*Warner et al.*, 2010] has been applied. The system couples the three-dimensional ROMS oceanic model and the SWAN wind wave generation and propagation model. In order to simplify the analysis and focus the study on wave-current interaction, the atmospheric forcing was derived from the results of the WW3 model, keeping the WRF module deactivated.

3.1. The Hydrodynamic Model

[13] The three-dimensional ROMS hydrodynamic model, including the vortex-force formulation for the interaction of surface gravity waves and currents, was used to achieve a detailed characterization of the flow regime in the study area. ROMS is a three-dimensional, free-surface, terrain-following numerical model that solves finite difference approximations of the Reynolds Averaged Navier-Stokes (RANS) equations using the hydrostatic and Boussinesq assumptions [*Chassignet et al.*, 2000; *Haidvogel et al.*, 2000] with a split-explicit time stepping algorithm [*Shchepetkin and McWilliams*, 2005; *Haidvogel et al.*, 2008]. The wave-averaged momentum balance equations are based on the equations presented by *McWilliams et al.* [2004] and *Uchiyama et al.* [2010], which were implemented in the COAWST modeling system by Kumar et al. (submitted manuscript, 2011). The 3D primitive equations for the wave-averaged currents in horizontal orthogonal curvilinear and s terrain following vertical coordinate systems are given by the following equations.

x momentum balance:

$$
\underbrace{\frac{\partial}{\partial t}\left(\frac{H_z^c}{mn}u\right)}_{u-accel} + \underbrace{\frac{\partial}{\partial \xi}\left(\frac{H_z^c u}{n}u\right) + \frac{\partial}{\partial \eta}\left(\frac{H_z^c v}{m}u\right) + u\frac{\partial}{\partial \xi}\left(\frac{H_z u^{St}}{n}\right) + u\frac{\partial}{\partial \eta}\left(\frac{H_z v^{St}}{m}\right)}_{u-hadv}
$$

$$
+ \underbrace{\frac{1}{mn}\frac{\partial}{\partial s}(w_s u) + u\frac{\partial}{\partial s}\left(\frac{\omega_s^{St}}{mn}\right)}_{u-vadv} = \underbrace{-\frac{H_z^c}{n}\frac{\partial \phi^c}{\partial \xi}\bigg|_z}_{u-prsgrd} + \underbrace{\frac{H_z^c}{mn}fv}_{u-cor} + \underbrace{\frac{H_z^c}{mn}fv^{st}}_{u-stcor}
$$

$$
\underbrace{+H_z^c v^{st}\left(\frac{1}{n}\frac{\partial v}{\partial \xi} - \frac{1}{m}\frac{\partial u}{\partial \eta}\right)}_{u-hjvf} \underbrace{-\frac{1}{mn}w_s^{st}\frac{\partial}{\partial s}(u)}_{u-vjvf} \underbrace{+\frac{H_z^c}{mn}F^\xi}_{u-sstr+u-bstr} \underbrace{+\frac{H_z^c}{mn}F^{w\xi}}_{u-brk+u-rol} \underbrace{+\frac{H_z^c}{mn}D^\xi}_{u-hvisc}
$$
$$
\underbrace{\phantom{+H_z^c v^{st}\left(\frac{1}{n}\frac{\partial v}{\partial \xi}\right)\hspace{8cm}}}_{u-vf}
$$

$$
\underbrace{-\frac{\partial}{\partial s}\left(\overline{u'w'} - \frac{v}{H_z^c}\frac{\partial u}{\partial s}\right)}_{u-vvisc} \underbrace{+\widehat{F}^\xi}_{u-curv}
$$

(include $u-sstr$ and $u-bstr$ as boundary conditions)

$$(1)$$

y momentum balance:

$$
\underbrace{\frac{\partial}{\partial t}\left(\frac{H_z^c}{mn}v\right)}_{v-accel} + \underbrace{\frac{\partial}{\partial \xi}\left(\frac{H_z^c u}{n}v\right) + \frac{\partial}{\partial \eta}\left(\frac{H_z^c v}{m}v\right) + v\frac{\partial}{\partial \xi}\left(\frac{H_z u^{St}}{n}\right) + v\frac{\partial}{\partial \eta}\left(\frac{H_z v^{St}}{m}\right)}_{v-hadv}
$$

$$
+ \underbrace{\frac{1}{mn}\frac{\partial}{\partial s}(w_s v) + v\frac{\partial}{\partial s}\left(\frac{\omega_s^{St}}{mn}\right)}_{v-vadv} = \underbrace{-\frac{H_z^c}{m}\frac{\partial \phi^c}{\partial \eta}\bigg|_z}_{v-prsgrd} \underbrace{-\frac{H_z^c}{mn}fu}_{v-cor} \underbrace{-\frac{H_z^c}{mn}fu^{st}}_{v-stcor}
$$

$$
\underbrace{-H_z^v u^{st}\left(\frac{1}{n}\frac{\partial v}{\partial \xi} - \frac{1}{m}\frac{\partial u}{\partial \eta}\right)}_{v-hjvf} \underbrace{-\frac{1}{mn}w_s^{st}\frac{\partial}{\partial s}(v)}_{v-vjvf} \underbrace{+\frac{H_z^c}{mn}F^\eta}_{v-sstr+v-bstr} \underbrace{+\frac{H_z^c}{mn}F^{w\eta}}_{v-brk+v-rol} \underbrace{+\frac{H_z^c}{mn}D^\eta}_{v-hvisc}
$$
$$
\underbrace{\phantom{-H_z^v u^{st}\left(\frac{1}{n}\frac{\partial v}{\partial \xi}\right)\hspace{8cm}}}_{v-vf}
$$

$$
\underbrace{-\frac{\partial}{\partial s}\left(\overline{v'w'} - \frac{v}{H_z^c}\frac{\partial u}{\partial s}\right)}_{v-vvisc} \underbrace{+\widehat{F}^\eta}_{v-curv}
$$

(include $v-sstr$ and $v-bstr$ as boundary conditions)

$$(2)$$

continuity equation:

$$
\frac{\partial}{\partial t}\left(\frac{H_z^c}{mn}\right) + \frac{\partial}{\partial \xi}\left(\frac{H_z^c(u+u^{st})}{n}\right) + \frac{\partial}{\partial \eta}\left(\frac{H_z^c(v+v^{st})}{m}\right)
$$
$$
+ \frac{1}{mn}\frac{\partial}{\partial s}(w_s + w_s^{st}) = 0,
$$

$$(3)$$

where m^{-1} and n^{-1} are the Lamé metric coefficients; u, v, and w_s are the mean Eulerian components of velocity in the horizontal (ξ and η) and vertical (s) directions respectively; the vertical s coordinate is negative downward with $s = 0$ at mean sea level and $s = -1$ at the bottom; z is the vertical coordinate system positive upward with $z = 0$ at mean sea level; H_z^c is the grid-cell thickness; f is the Coriolis parameter; (F^ξ, F^η) represent the nonwave body forces and include the effect of the wind shear stress and bottom shear stress; $(F^{w\xi}, F^{w\eta})$ represent the nonconservative wave-induced accelerations, in this case the wave-breaking and roller-induced acceleration; and (D^ξ, D^η) are the parameterized horizontal momentum mixing terms. An overbar represents a time average, and a prime (') represents turbulent fluctuations. These equations are closed by parameterizing the Reynolds stresses $[(\overline{u'w'}), (\overline{v'w'})]$ using a turbulence-closure model. In this study we used the generic length-scale (GLS) method [*Umlauf and Burchard*, 2003] as implemented by *Warner et al.* [2005]. In this method the bottom shear and surface shear stresses are included as boundary conditions.

[14] The Stokes velocity components (u^{st}, v^{st}, w^{st}) are defined for monochromatic waves by

$$
\overrightarrow{u_\perp^{st}} = (u^{st}, v^{st}) = \left(\frac{A^2}{2\sin h^2[\mathcal{H}]}\cos h[2\mathcal{H}(1+s)]k_\xi,\right.
$$
$$
\left.\frac{A^2}{2\sin h^2[\mathcal{H}]}\cos h[2\mathcal{H}(1+s)]k_\eta\right),
$$

$$(4)$$

$$
w^{st} = -\overrightarrow{\nabla_\perp} \cdot \left(\int_{-1}^{s} H_z^c \overrightarrow{u_\perp^{st}}\, ds'\right),
$$

$$(5)$$

where $\overrightarrow{\nabla_\perp}$ is the horizontal differential operator vector; $\perp$ represents the horizontal part of the 3-D vector, and the upper arrows represent vector quantities.

[15] The vertical motion past the s surfaces is the sum of the Eulerian and Stokes vertical motions ($w_s^l = w_s + w_s^{st}$) and is given by

$$w_s^l = w_s + w_s^{st} = \left[(w + w^{st}) \right.$$
$$\left. - \left(\frac{\partial z}{\partial t} + m(u + u^{st}) \frac{\partial z}{\partial \xi} + n(v + v^{st}) \frac{\partial z}{\partial \eta} \right) \right] \Bigg|_s, \quad (6)$$

and the vertical mass flux is calculated as

$$W^l = \frac{w_s^l}{mn} = \int_{-1}^{s} \left(\frac{\partial}{\partial \xi} \left(\frac{H_z^c}{n} (u + u^{st}) \right) + \frac{\partial}{\partial \eta} \left(\frac{H_z^c}{m} (v + v^{st}) \right) \right) ds'$$
$$- \frac{1}{mn} \cdot \frac{z + h}{\zeta + h} \cdot \frac{\partial \zeta^c}{\partial t}. \quad (7)$$

In the momentum balance equations (equations (1) and (2)), the first term represents the local acceleration (accel), terms two and three are the horizontal advection terms (hadv), and the fourth term is the vertical advection (vadv). On the right-hand side of the equations, the first term represents the total pressure gradient (prsgrd), the second is the Coriolis acceleration (cor), and the third is the Stokes-Coriolis (stcor) acceleration. The next two terms (hjvf + vjvf) are the horizontal and vertical vortex forces. The surface shear stress (sstr) and bottom shear stress (bstr) are considered in the fifth term. The next term includes the wave-breaking-induced (break) and roller-induced (rol) forces. The following two terms represent the horizontal (hvisc) and vertical (vvisc) mixing terms. The last term (*curv*) is the curvilinear metric term, which in the case of a Cartesian grid is equal to zero (the expression of this term for orthogonal curvilinear grids is given by Kumar et al. (submitted manuscript, 2011)). This nomenclature is used in the following sections when analyzing the leading terms of the momentum balance in Willapa Inlet.

[16] The geopotential function ϕ^c (which has absorbed the Bernoulli Head $\mathcal{K}$) is evaluated from the integration of the vertical momentum equation [*Uchiyama et al.*, 2010]:

$$\phi^c = g\left(\zeta^c - \widehat{\zeta} \right) - (P - \mathcal{K})|_{\zeta^c} + \int_s^0 \left[\frac{g\rho}{\rho_0} \right] H_z^c ds + \underbrace{\int_s^0 [-K] H_z^c ds}_{vkvf}, \quad (8)$$

where ρ and ρ_0 are total and reference densities, respectively; g is acceleration that is due to gravity; P is the wave-average surface pressure correction term [see *McWilliams et al.*, 2004] and is defined as

$$P = \frac{gA^2}{2\sigma} \left\{ \frac{\tanh[\mathcal{H}]}{\sinh[2\mathcal{H}]} \left(-\frac{1}{H_z^c} \frac{\partial \mathcal{V}}{\partial s} \Big|_{s=0} + \cosh[2\mathcal{H}] \frac{1}{H_z^c} \frac{\partial \mathcal{V}}{\partial s} \Big|_{s=-1} \right. \right.$$
$$\left. \left. + \int_{-1}^0 \frac{1}{H_z^c} \frac{\partial^2 \mathcal{V}}{\partial s'^2} \cosh[2kD(s'+1)] ds' \right) \right\} - \frac{gA^2}{\sigma} k \tanh[\mathcal{H}] \mathcal{V} \Big|_{s=0} \quad (9)$$

where

$$\mathcal{V} = \overrightarrow{k} \cdot \overrightarrow{u}, \quad (10)$$

$\overrightarrow{k}$ is the wave number vector and k is the magnitude; $\sigma = \sqrt{gk\tanh[\mathcal{H}]}$ is the intrinsic frequency.

[17] The Bernoulli Head ($\mathcal{K}$) is defined as

$$\mathcal{K} = \frac{1}{4} \frac{\sigma A^2}{k \sin h^2[\mathcal{H}]} \int_{-1}^0 \frac{1}{H_z^c} \frac{\partial^2 \mathcal{V}}{\partial s'^2} \sin h[2kD(s - s')] ds', \quad (11)$$

$\zeta^c = \zeta + \widehat{\zeta}$ is the composite sea level. ζ represents the sea level, and $\widehat{\zeta}$ is the quasi-static sea level component defined by

$$\widehat{\zeta} = \frac{-P_{atm}}{g\rho_0} - \frac{A^2 k}{2 \sin h[2\mathcal{H}]}, \quad (12)$$

where $\mathcal{H}$ is the relative water depth defined as

$$\mathcal{H} = k\left(h + \zeta + \widehat{\zeta} \right) \equiv kD, \quad (13)$$

P_{atm} is the atmospheric pressure over the sea surface; $D = (h + \zeta + \widehat{\zeta})$ is the wave-averaged thickness of the water column, h is the resting depth, and A is the wave amplitude.

[18] The last term in geopotential equation (4) represents the vertical vortex force, where

$$K = \overrightarrow{u_\perp^{st}} \cdot \left(\frac{1}{H_z^c} \frac{\partial \overrightarrow{u_\perp}}{\partial s} \right) = (u^{st}, v^{st}) \cdot \frac{1}{H_z^c} \frac{\partial(u,v)}{\partial s}. \quad (14)$$

The total pressure gradient force ($\overrightarrow{P^{tot}}$) is equal to the horizontal gradient of the geopotential function after extracting the vertical vortex force and can be decomposed into the current contribution ($\overrightarrow{P^c}$), the quasi-static response ($\overrightarrow{P^{qs}}$), the Bernoulli Head term ($\overrightarrow{P^{bh}}$), and the surface pressure boundary correction ($\overrightarrow{P^{pc}}$):

$$\underbrace{\overrightarrow{P^{tot}}}_{prsgrd} = \underbrace{-\overrightarrow{\nabla}_\perp \left(g\zeta^c + \int_s^0 H_z^c \frac{g\rho}{\rho_0} ds \right)}_{\overrightarrow{P^c}} + \underbrace{g\overrightarrow{\nabla}_\perp \widehat{\zeta}}_{\overrightarrow{P^{qs}}} + \underbrace{\overrightarrow{\nabla}_\perp \mathcal{K}|_{\zeta^c}}_{\overrightarrow{P^{bh}}} + \underbrace{\overrightarrow{\nabla}_\perp P|_{\zeta^c}}_{\overrightarrow{P^{pc}}}. \quad (15)$$

[19] In these equations the effects of surface waves on the hydrodynamics are included by different conservative and nonconservative wave forces. The wave forces considered in the present study are the following:

[20] 1. Conservative wave forces: The vortex force (VF = hjvf + vjvf + vkvf) and the Bernoulli Head (BH = $\mathcal{K}$) are the conservative wave forces included in ROMS. The former represents the current vorticity advection by the Stokes Drift. The Bernoulli Head is essentially an adjustment to the pressure in accommodating incompressibility [*Lane et al.*, 2007].

[21] 2. Nonconservative wave forces: Different types of wave-induced nonconservative wave acceleration and dissipation terms were considered. The depth-induced wave breaking and the whitecapping create flow accelerations (BRK). These accelerations are dependent on the energy dissipated during the breaking process. The specific formulations used to represent the wave-breaking-induced accelerations are presented in Appendix A. We assumed that all the energy dissipated in the wave-breaking process is transferred to

the mean flow and turbulence. Surface rollers and bottom streaming were not considered. Wave-induced dissipation terms include the enhancement of the apparent bed roughness that is due to the effect of the turbulence in the wave boundary layer (KAW) and the turbulent kinetic energy injection during the wave breaking (TKE). In this study the enhancement of the apparent bed roughness was parameterized using the formulation proposed by *Madsen* [1994], which results in a modification of the bottom shear stress vector. Part of the energy dissipated during wave breaking is transformed into turbulent kinetic energy that is a source of turbulence in the sea surface. This is introduced as a surface flux of turbulence kinetic energy in the GLS method [*Warner et al.*, 2005], affecting the vertical viscosity terms. As done by M. Olabarrieta et al. (Ocean-atmosphere dynamics during Hurricane Ida and Nor'Ida: An application of the coupled ocean-atmosphere-wave-sediment transport (COAWST) modeling system, submitted to *Ocean Modelling*, 2011), the surface flux was considered to be proportional to the net energy dissipated during the breaking process [*Feddersen and Trowbridge*, 2005] and the surface roughness proportional to the significant wave height [*Stacey*, 1999]. The formulations used are presented in Appendix C.

3.2. The Wave Generation and Propagation Model

[22] The modification of the momentum equations to include the effects of surface waves requires information on the properties of wave height, wave energy dissipation, propagation direction, and wavelength. Other algorithms, such as the bottom boundary modules and turbulence submodels, also require wave information such as period and bottom orbital velocity. These quantities are obtained from Simulating Waves Nearshore (SWAN) [*Booij et al.*, 1999], a wave-averaged model that solves transport equations for wave action density N and accounts for shoaling and refraction, wind wave generation, wave breaking, bottom dissipation, and nonlinear wave-wave interactions. SWAN can be run concurrently with the circulation model with two-way coupling, whereby currents and sea surface elevations influence the wavefield and waves affect the circulation. In the COAWST modeling system ROMS feeds SWAN with the free-surface elevations (ELV) and currents (CUR). The currents are computed according to the formulation presented by *Kirby and Chen* [1989], in which the vertical distribution of the current profile is taken into account, as well as the relative water depth of surface waves (Olabarrieta et al., submitted manuscript, 2011). For a more complete description of the coupled system the reader is referred to the work of *Warner et al.* [2008].

[23] The effects of each process described above are analyzed in section 6, referring to each term with the nomenclature defined in this section.

4. Model Setup

[24] This study was focused on the time period between 22 and 29 October 1998, which included a storm event. Wave conditions measured by the closest NOAA buoy during this time are shown in Figure 2a. Typical nonstorm wave conditions consisted of 1–2 m wave heights. During the storm on 24 October, waves increased to 5 m significant wave height. The peak period in this storm event was approximately 16 s, corresponding to a swell coming from the WSW. During

the storm the wind speed increased to approximately 12 m/s and was from the SSE-SSW (Figure 2b). This storm was associated with a cyclone propagating toward the U.S. west coast. After the passage of the cyclone an abrupt front followed by an anticyclone hit the study area, generating the few other minor events observed on 27 and 28 October. During this period the winds were from the NW-WNW and the waves were from the WNW.

[25] For the wave modeling, a system of three nested grids was used to simulate the wind wave generation and propagation (see Figure 3). The most exterior grid (PACF), with a resolution of 0.1°, extended all over the North Pacific Ocean (Figure 3a). The intermediate grid (WASH) covered the region between −127°W and −123.77°W and 45.1°N and 47.98°N and had a 4 km resolution (Figure 3b). The highest-resolution grid (WILL) was discretized using a grid composed of 528 × 796 cells in the horizontal, with a 75 m constant resolution over the whole computational domain (Figure 3c). The bathymetric grid within the estuary was interpolated from a finite element model grid developed by the U.S. Army Corps of Engineers, Seattle District, who resurveyed most of the subtidal area of the bay in 1998 [*Kraus*, 2000a, 2000b]. This bathymetry was merged with the GEBCO08 bathymetric data to increase the offshore extension of the computational domain (see Figure 3c). A Joint North Sea Wave Project (JONSWAP) spectrum along the open boundary of the PACF domain was considered, and the spectral parameters were derived from WWIII reanalysis results. For the analysis period, no directional wave spectra are available in the WWIII database. A 1.25° horizontal and 3 h temporal resolution wind forcing from the same database was imposed in PACF and WILL domains, while for the WASH grid higher temporal resolution winds measured by a meteorological station located in Willapa Bay were used. The time evolutions of the directional wave spectra were stored every hour in the points located on the boundaries of WASH and WILL domains. To characterize the wind wave spectra, 25 frequency (0.01–1 Hz) and 36 directional bands were used in PACF, 40 and 72 in WASH, and 40 and 90 in WILL. In all domains the exponential energy transfer from the atmosphere to the wind wavefield was parameterized using the closure model presented by *Komen et al.* [1984].

[26] The numerical grid used for the hydrodynamic model had the same characteristics as the horizontal grid used in WILL domain and had 10 terrain-following (sigma) levels in the vertical. In ROMS, the Nikuradse roughness (K_s) was considered constant over the whole simulation domain with a value equal to 0.05 m. Salinity and temperature were held constant at S_0 = 35 ppt and T_0 = 21°C. Subgrid scale parameterizations for the mixing of momentum and scalars were accomplished with the Generic Length Scale two-equation turbulence (*Umlauf and Burchard* [2003], as implemented by *Warner et al.* [2005]) parameterized as the K-ε model. Boundary conditions for tides were derived from the ADCIRC [*Luettich et al.*, 1992] tidal database for the eastern Pacific region [*Spargo et al.*, 2004]. This database includes water levels and current velocity phases and amplitudes of the M2, S2, N2, K2, O1, K1, Q1, and P1 tidal constituents along west coast of the United States. Tidal elevations and currents were interpolated from the ADCIRC grid to the ROMS grid computational boundaries. A Flather
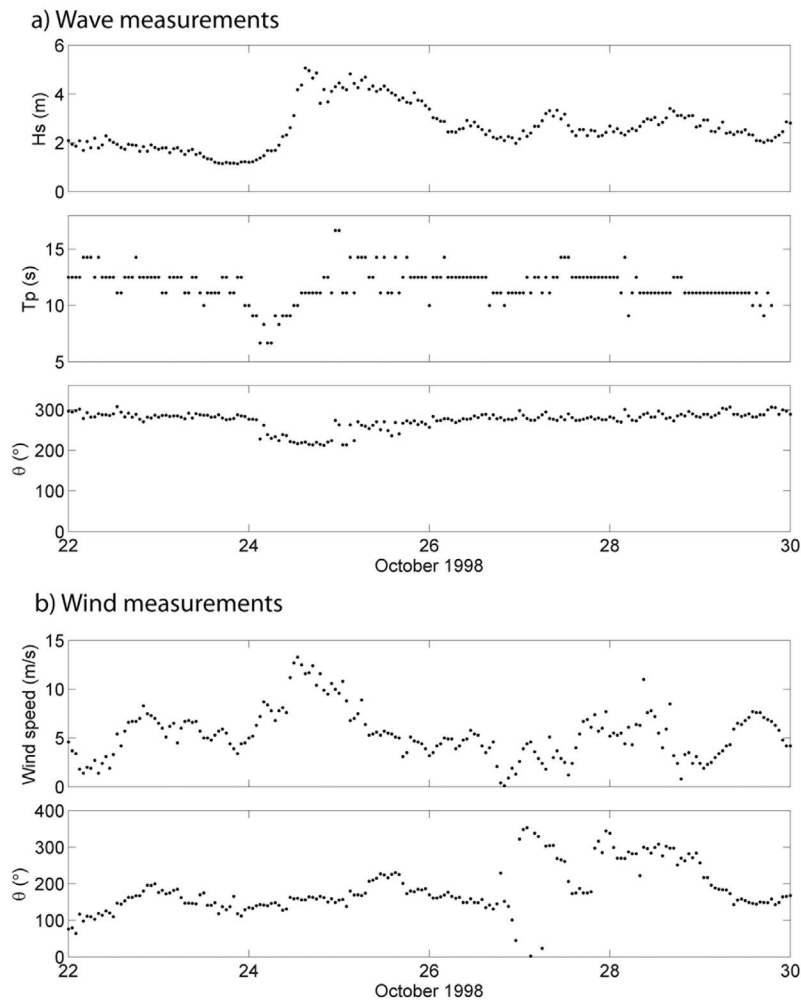
Figure 2. (a) Time variation of wave conditions measured by the 46029 NOAA buoy during the analysis period. The top plot indicates the significant wave height, the middle plot indicates the peak period variation, and the bottom plot shows the peak wave direction (nautical convention). (b) Wind conditions measured by the 46029 NOAA buoy during the analysis period. The top plot indicates the time variation of the wind intensity while the bottom plot shows wind direction (nautical convention).

boundary condition [*Flather*, 1976] for the barotropic currents was imposed in the three open boundaries of the study domain. This boundary condition allows the free propagation of the astronomic tides as well as the propagation of the wind generated currents. Taking into account that the tidal flux is at least one order of magnitude higher than the river flux, river inputs were not considered.

[27] In the coupled WILL domain, different time steps were used for ROMS and SWAN. In ROMS a 10 s baroclinic time step was used with a mode-splitting ratio of 20. SWAN was run with a time step of 300 s. The same data exchange rate between ROMS and SWAN was used.

5. Evaluating Model Performance

[28] In this section the wave results obtained in the WASH grid are compared with the NOAA 46029 wave buoy measurements (location shown in Figure 3b). The results of a fully coupled ROMS-SWAN system for the WILL grid during the period from 22 to 29 October are also compared

with observed sea surface elevations, barotropic currents, and waves (measurements acquired by the U.S. Army Corps of Engineers during the years 1998–1999 in Willapa Inlet). In order to evaluate the model performance, all the processes utilized in wave-current interaction were activated in the simulation. These were described in section 3 and include the effect of the three-dimensional vortex force (VF) and the Bernoulli Head (BH), the accelerations induced during the wave breaking (BRK), the bottom roughness enhancement (KAW) that was due to the increase of the turbulence in the wave boundary layer, and the turbulence injection (TKE) in the sea surface that was due to wave breaking. The effects of currents on the wave propagation and generation (ELV and CUR) were also considered. This run will be referred to as Run1. We compared model results with those of four of the stations: St1, St2, and St3 were located in the inlet zone, and station St4 was located inside the estuary. Figure 3c depicts the location of each station and the bathymetry of the study region. As explained by *Smith et al.* [2000], site St1 was located seaward of Willapa bar and sites St2 and St3 were
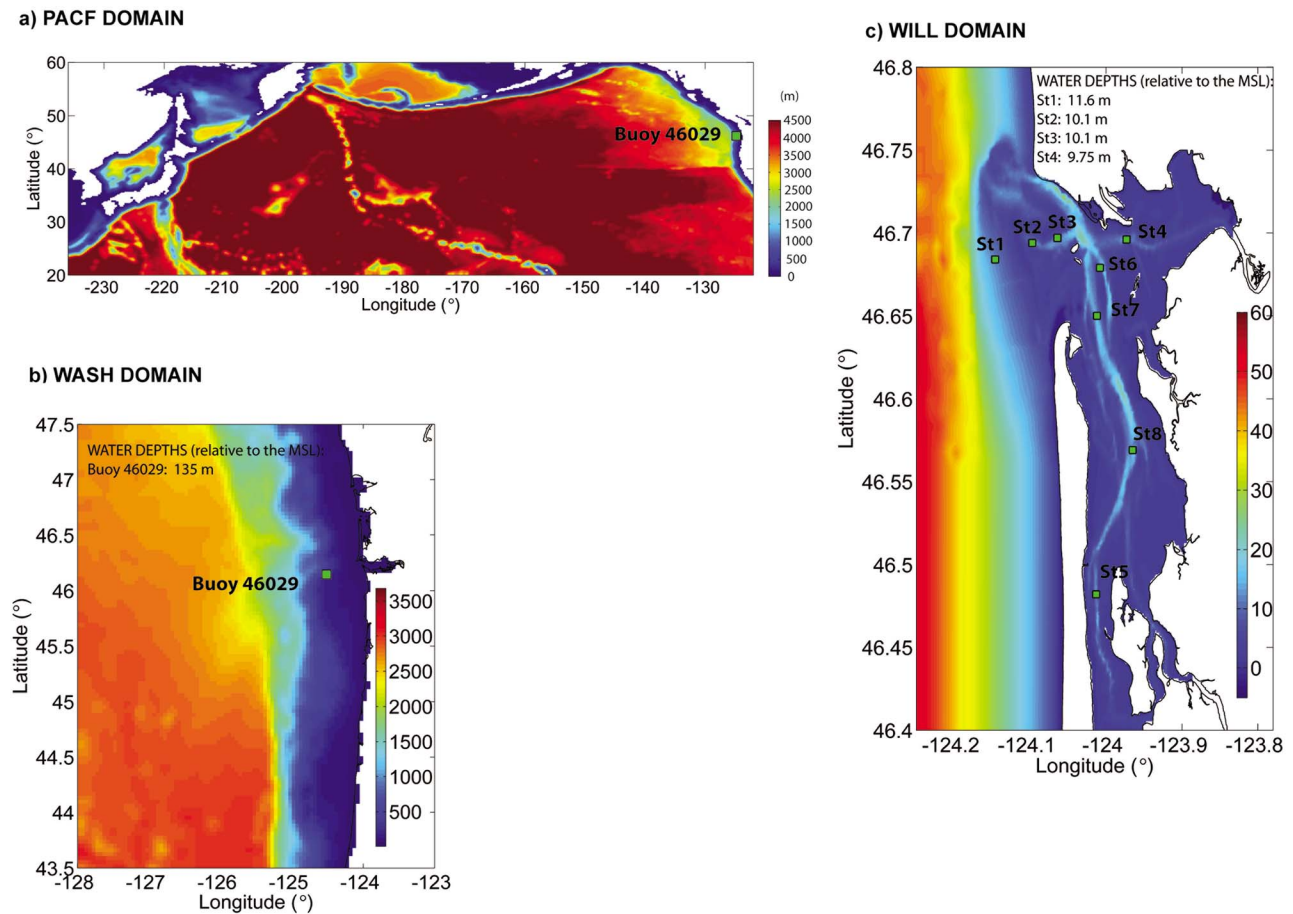
Figure 3. Numerical grid domains and the corresponding bathymetry (meters relative to the MSL). (a) PACF grid, with a resolution of 0.1°, extended over the North Pacific Ocean. (b) The intermediate WASH grid covered the region between −127°W and −123.77°W and 45.1°N and 47.98°N and had a 4 km resolution. (c) The WILL domain covered Willapa Bay and had a constant horizontal resolution of 75 m. The green dots indicate the measurement stations deployed by the U.S. Army Corps of Engineers during the period 1998–1999 as well as other stations used to analyze the numerical results (St5, St6, St7, and St8).

located landward of the bar. Wave measurements were obtained at St1, St2, and St3 by Paroscientific bottom-mounted pressure sensors and acoustic Doppler velocimeters in mean water depths of approximately 10 m, resolving wave motions with periods down to 3.5–4 s. Inside the estuary, at St4, current velocities were measured with acoustic Doppler velocimeters. Bottom-mounted pressure gauges were used to measure tidal elevations. The coherence between the model measurements was analyzed in terms of the root-mean-square error (RMSE), correlation coefficient (R), and model performance (skill, S) [Wilmott, 1981]. In Appendix D the formulations used for each parameter are specified. The rest of the stations indicated in Figure 3c were used to analyze the numerical results (no measurements were acquired in these locations).

5.1. Waves

[29] WASH results were verified by comparing the modeled wave spectra with the NOAA 46029 wave buoy measurements. Figure 4a shows the comparison of the significant wave height and peak period time evolution for the WASH domain. Although a good agreement between the simulated H_s (significant wave height) and T_p (peak period) and the measurements was obtained ($S = 0.9$ and $S = 0.52$ respectively), the simulated time series was smoother than the measurements and did not reproduce some peaks observed in the measured signal. Before the peak of the storm, the computed H_s was 0.7 m higher than the measurements.

[30] Comparing the measured winds with those provided by WW3 we identified that the overestimation was a consequence of an overprediction of the wind intensity. However, during the peak of the storm, the opposite occurred and waves were underestimated by about 1 m. Figure 4b compares the measured and computed wave spectra in different time instants. As indicated by the model skill and correlation coefficient values, in general a good agreement between the measured and computed spectra was obtained, indicating that the WASH run was reproducing correctly the wave generation and propagation process in the study domain. The differences obtained for 25 October were caused by the underestimation of the wind intensity during the peak of the storm.
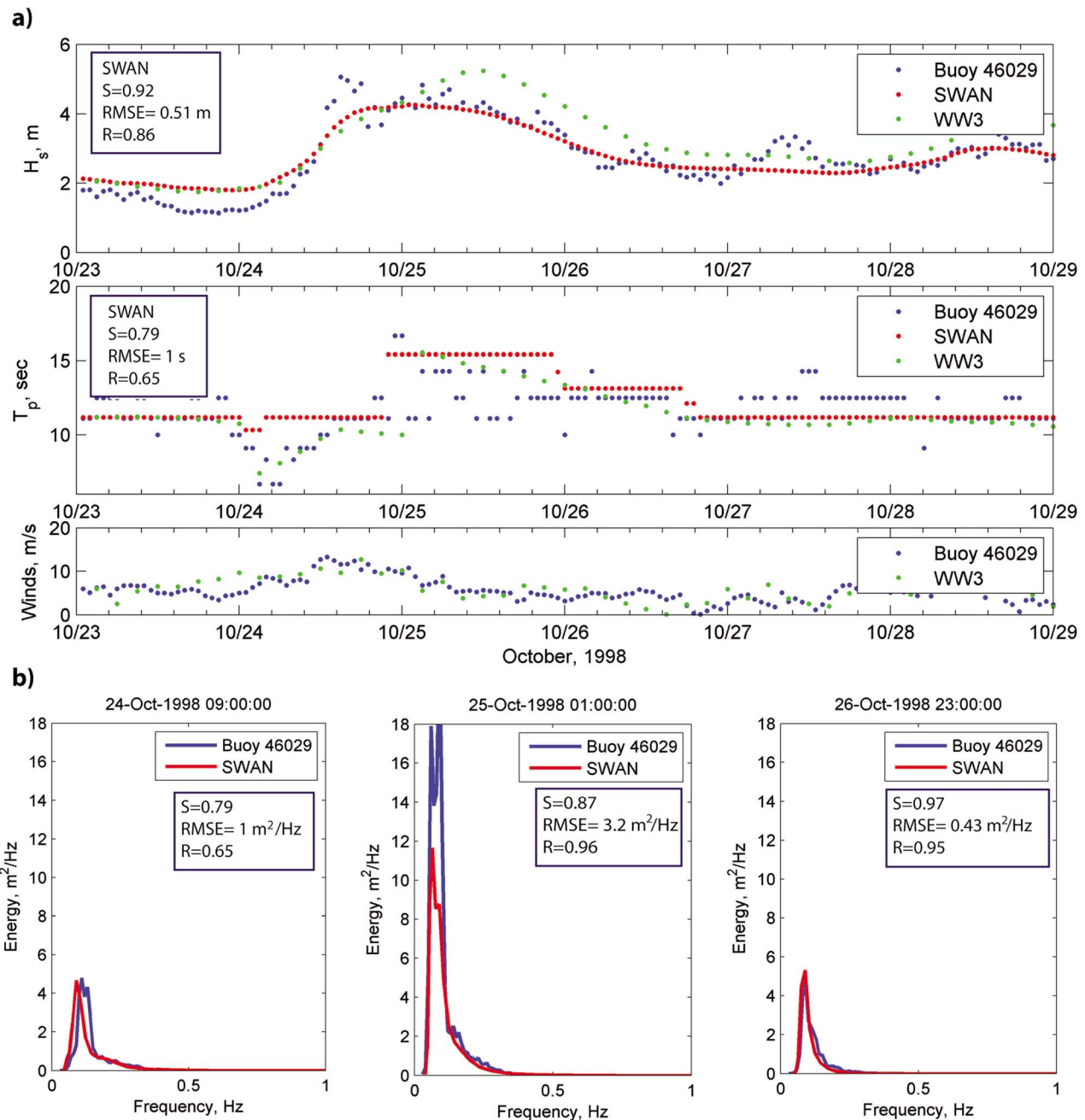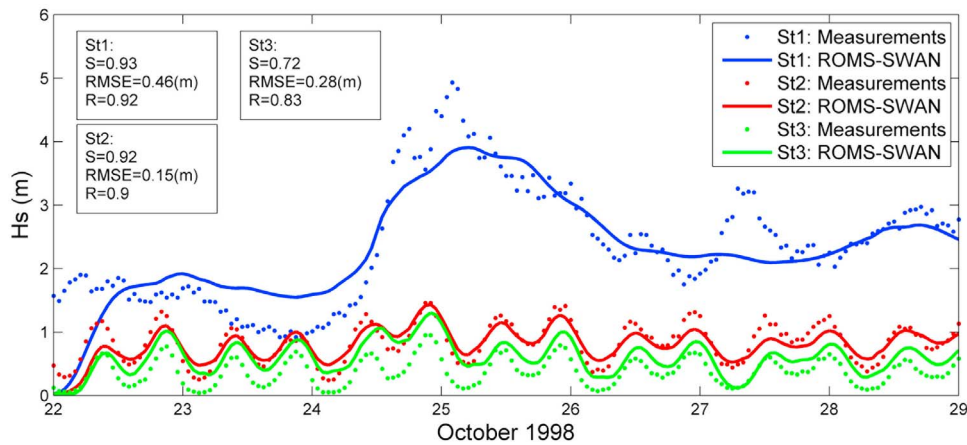
Figure 4. Comparison of the computed and measured (a) significant wave heights and peak period time evolution and (b) wave spectra in the location of the 46029 NOAA buoy. The numerical results are those computed in the WASH domain.

[31] Figure 5 depicts the comparison of computed (WILL grid) and measured significant wave heights in the inlet stations. It is noteworthy that at St1, located in water depths of 11.6 m, a small fraction of the waves (0.5%) were breaking during the peak of the storm with the measured signal very similar to that modeled in the NOAA buoy location. The underprediction of the significant wave height in the peak of the storm, as explained earlier, was a consequence of the underestimation of the wind intensity by WWIII.

[32] At St1 the significant wave height varied considerably between the storm and less-energetic periods. In the interior stations (St2 and St3) the significant wave height was greatly reduced and showed a modulation with a period of 12.4 h.

[33] At these stations, the variations of the significant wave height during calm and storm periods were small. This observation suggested that waves propagating from the offshore were constantly breaking over the ebb shoal. Because of the energy dissipation process that results from wave breaking, only a limited amount of wave energy was able to penetrate into the inlet. Since during the low tide the water depth in the ebb shoal is lower than during the high tide, the intensity of energy dissipation was more severe
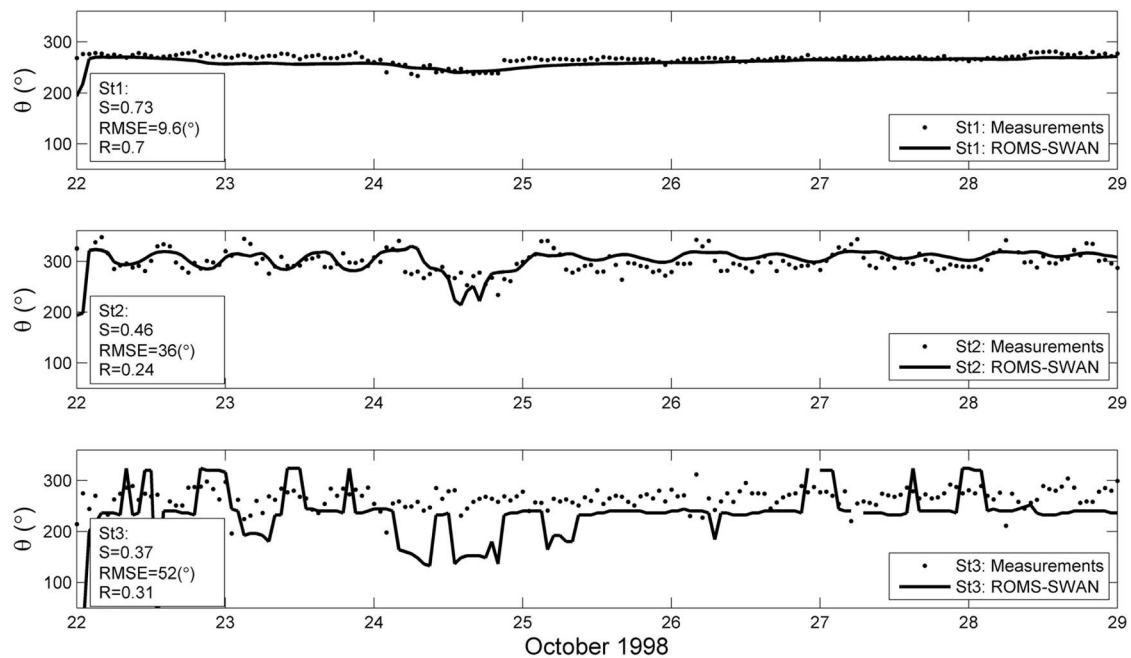
Figure 5. Comparison of the computed and measured significant wave heights in those stations located in the inlet.

during the low tide and therefore less wave energy was able to propagate inside the inlet to reach stations St2 and St3.

[34] The peak wave directions (see Figure 6) were correctly predicted at station St1, while at St2 and St3 there was a bigger discrepancy. Results from both the simulations and measurements indicated that during the simulation period, waves were from the west except between days 24 and 25, when waves were more from the WSW. At station St2 a higher variability of the peak direction than in site St1 was observed. The most remarkable feature of the peak wave direction signal in station St2 is the tidal modulation observed during nonstorm conditions. During the ebb, waves were from west while during the flood the direction changed to NNW. This was correctly reproduced by the model, although tidally induced variations were less intense in the model than in the observations.

[35] On 24 October a change in the peak direction occurred to be more aligned with the local winds, indicating that locally generated sea became relevant in that station. The measurements in station St3 showed that the peak direction was also tidally modulated. During 24 October the tidal modulation was not as important as during the rest of the analysis period. The comparison between measured data and computed results showed that the numerical model is not able to correctly capture the change of the peak direction observed in the measurements. Between 22 and 27 October, winds were mainly from the SSW, alternating with periods of SSE winds. These winds generated short waves both outside and inside the estuary. Outside the estuary, low-frequency swells propagated toward the coast. In the inlet, where most of the offshore energy was dissipated, depending on the wind intensity and on the capacity of penetration

Figure 6. Comparison of the computed and measured peak directions in those stations located at stations St1, St2, and St3 in the inlet.
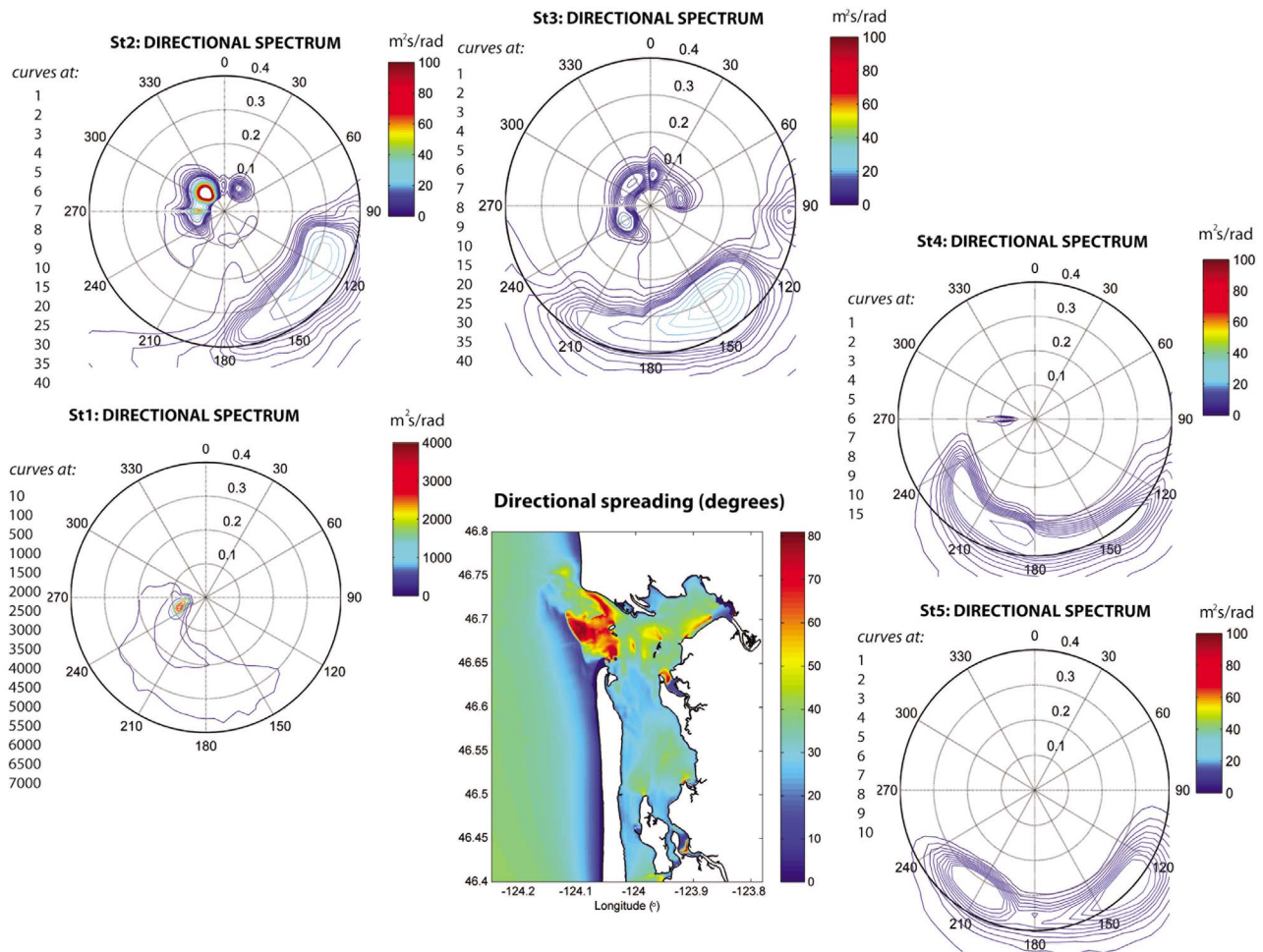
Figure 7. Spatial distributions of the simulated directional wave spectra, 24 October, during the maximum ebb. Notice the scale change between the station St1 and the rest of the stations.

of the swell, local sea can be dominant over the swell and vice versa. To further investigate the spatial variation of the wave direction, Figure 7 shows the spatial distribution of the simulated wave spectra for 24 October during the maximum ebb offshore of the inlet (St1), in the inlet zone (St2 and St3), and inside the estuary (St4). One more point (St5), located in the Nahcotta channel (see Figure 2), was considered in order to analyze the wave conditions inside the estuary. Figure 7 (middle) shows the directional spreading computed in SWAN.

[36] At St1 the main energy source was the swell (0.05–0.15 Hz) with directions between 240 and 270. At St2 and St3, in the swell band, a double peak in directions was observed. This was the consequence of the refraction created by the shoal. The energy refracted from the WSW and from the WNW in the ebb shoal was concentrated at those stations, and therefore a double peak was detected. At these stations the directional spreading was higher than in St1 and the swell energy was lower than in St1 because waves had already broken. A third peak was also detected in these stations, with a frequency of 0.3 Hz, corresponding to the sea generated inside the estuary, with a much lower energy content and with directions of about 120°–180°. In the stations located inside the estuary, the wave energy was concentrated on the high-frequency band (0.3–0.4 Hz) with no energy in the swell band. Therefore, it can be concluded that inside the estuary the locally generated sea was the only wave energy source. This was characterized by a high directional spreading with directions between 110° and 240°.

[37] It is important to point out that St3 was located in the transition zone between the swell-dominated region and the sea-dominated region. For that reason the correct representation of waves in this specific station is very challenging. The differences between computed peak wave directions and observations could be caused by simplifications introduced in the model such as a spatially uniform wind field or differences in the bathymetry considered in the numerical simulations and the effects of its discretization.

[38] It can be concluded that with regard to the wave simulation, the comparison of the significant wave heights showed that there was a good agreement between the observations and computed results, being the minimum obtained skill coefficient of 0.72. The agreement between computed and measured peak wave directions was not as good as in the case of the significant wave height. However, the model reproduced the tidally induced modulation but the variations in the model were smaller than the measured ones. The biggest differences between observed and computed values

were obtained for site St3, with a minimum skill coefficient of 0.37 (St3). These were attributed to the fact that this station was located in the transition zone between the offshore-dominated region and the inshore-sea-dominated area.

5.2. Sea Surface Elevations and Currents

[39] Figure 8a depicts the observed and simulated tidal elevations at the stations located in the inlet (St1–St3) and inside the estuary (St4). During this period the predicted sea levels agreed well with the observations. The model correctly reproduced the tidal amplitude and also the tidal phase. The mean tidal prism for the analysis period was estimated at 5.5×10^8 m^3. Comparing the numerical results with and without considering the wind shear stress in the hydrodynamic model (not shown), we concluded that in the stations located landward of the ebb shoal, the main contribution of residual tide during the peak of the storm was the wave setup. The wind effect was negligible in comparison with the wave setup and the astronomic tides.

[40] In the inlet, barotropic currents were mainly driven by tides, with the M2 constituent the most relevant component. The maximum barotropic velocities were observed in St2, where the measured intensity reached up to 1 m/s (Figure 8b). St1 was the one with the weakest currents, with maximum observed currents of 0.5 m/s. In all the cases the dominant component of the velocity was the eastward component (U), although in St2 the northward component (V) was also relevant. In sites St1 and St3 the RMSE of the current module was approximately 0.1 m/s, while in St2 the RMSE increased to 0.15 m/s. In this station the eastward current amplitude was overestimated while the northward component's amplitude was underestimated. This could be caused by the bathymetry discretization. The results of the numerical model are the average velocities in a grid cell with 75 m side length, while the measurements are characteristics of a single point. However, in all the stations the time variation of both components was correctly estimated (see Figure 8b).

[41] The vertical structure of the current profiles was mainly barotropic. Figure 9 depicts the comparison between northward and eastward current profiles in St2. Figure 9 (top) represents the tidal phase that corresponds to each profile, indicated with a dot with a given color. In Figure 9 (bottom left and bottom right) both components of the profiles are shown, with colors corresponding to Figure 9 (top). Dotted lines represent measured profiles while continuous lines are computed profiles.

[42] In Table 1 the coherence between the modeled and measured profiles in terms of RMSE, R, and model skill are indicated. In general a good agreement between observations and computed profiles was achieved, although some differences between current phases were observed in some instances. Measured current profiles did not exhibit a strong vertical shear during any part of the tidal cycle. In spite of the computed phase difference, the shape of the current profiles was correctly reproduced by the numerical model.

[43] In summary, results identified that sea surface time variations were correctly simulated in all the considered stations, with the minimum skill coefficient of 0.99. The comparison of barotropic currents showed that in general the model was giving reasonable results with minimum values in station St1 of 0.37. In the rest of the stations the skill was higher than 0.87. The station with the highest RMSE was St2, with values of 0.15 m/s. The vertical profiles also showed acceptable skill and correlation coefficients. Most of the observed differences were attributed to a phase difference between observations and computed profiles and not to the shapes of the profiles themselves.

6. Wave-Current Interaction in Willapa Inlet-Estuary System

[44] The consistency between simulated waves and currents in Willapa Bay indicated that the ROMS-SWAN numerical system could be a useful tool to analyze the effects of different physical processes in the inlet-estuary system. In this section we studied the effects of wave-current interaction, focusing on the specific effect of the conservative and nonconservative wave forces, including VF, BH, BRK, KAW, and TKE. The closure models for each of these terms were specified in section 3. The analysis of wave's effect on the current field was performed by comparing the momentum balance in different tidal phases between simulations with and without considering the wave forces. The effects of the sea surface elevation variations (ELV) and currents (CUR) on wave propagation were also studied by comparing different numerical runs in which these terms were switched off. Table 2 summarizes the characteristics of the performed numerical simulations, indicating which processes or terms in the equations were considered.

[45] Run R0 considered only tidal wave propagation and wind effect. The base run R1, used in section 5 (model verification), considered all the processes relevant to wave-current interaction. Waves were imposed at exterior boundaries and were also locally generated by wind. During the propagation and generation processes, waves were affected by water level changes as well as by currents. With regard to the circulation, all the forcing (VF, BH, and BRK) and dissipation terms induced by waves (KAW and TKE) were taken into account. In run R2 waves were not affected by currents, either in the propagation and generation processes. R3 did not take into consideration either the effect of water level variations or the effect of the currents on the waves. In R4 all wave-current interaction processes were considered except of the enhancement of the apparent bottom roughness.

6.1. Effect of Waves on the Hydrodynamics: Momentum Balance Analysis

[46] The tidal cycle corresponding to the peak of the storm was selected to analyze the influence of waves on inlet hydrodynamics. The effect of waves on the barotropic momentum balance in different tidal phases was analyzed first, followed by their effects on mean sea levels and barotropic currents. At the end of this section the possible wave-induced baroclinic effects are discussed.

[47] *Hench and Luettich* [2003] analyzed the transient momentum balances in an idealized shallow tidal inlet as well as for Beaufort Inlet (North Carolina). Their results showed that momentum balances in the immediate vicinity of these inlets vary significantly in time and space and oscillate between two dynamical states. Near maximum ebb or flood, along-stream momentum balances are dominated by advective acceleration, pressure gradient, and bottom

a) Sea surface elevation
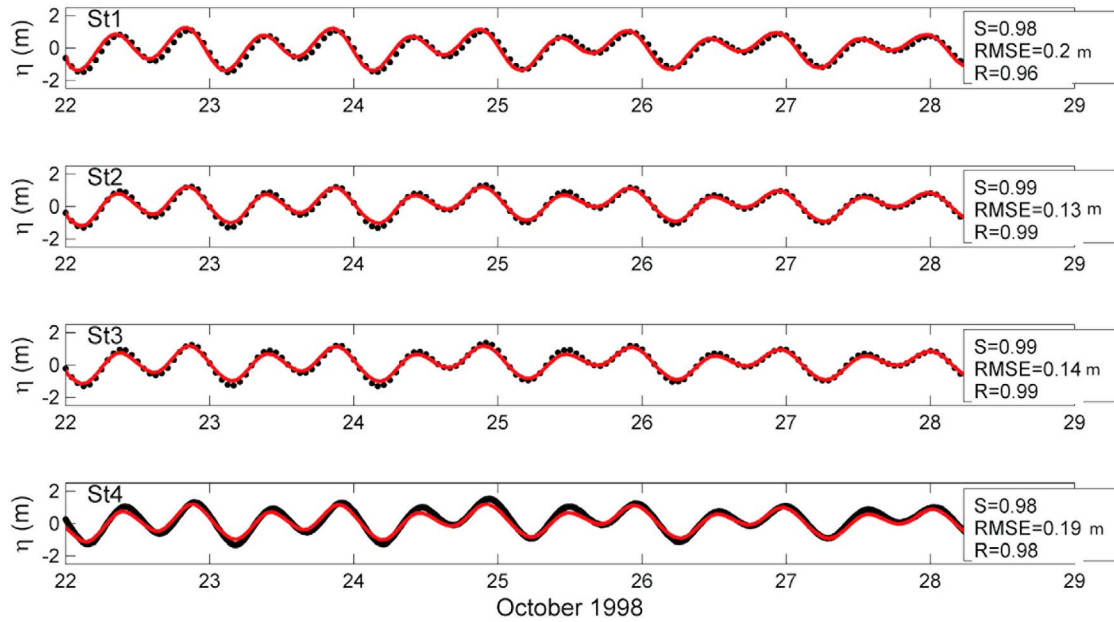
b) Barotropic currents
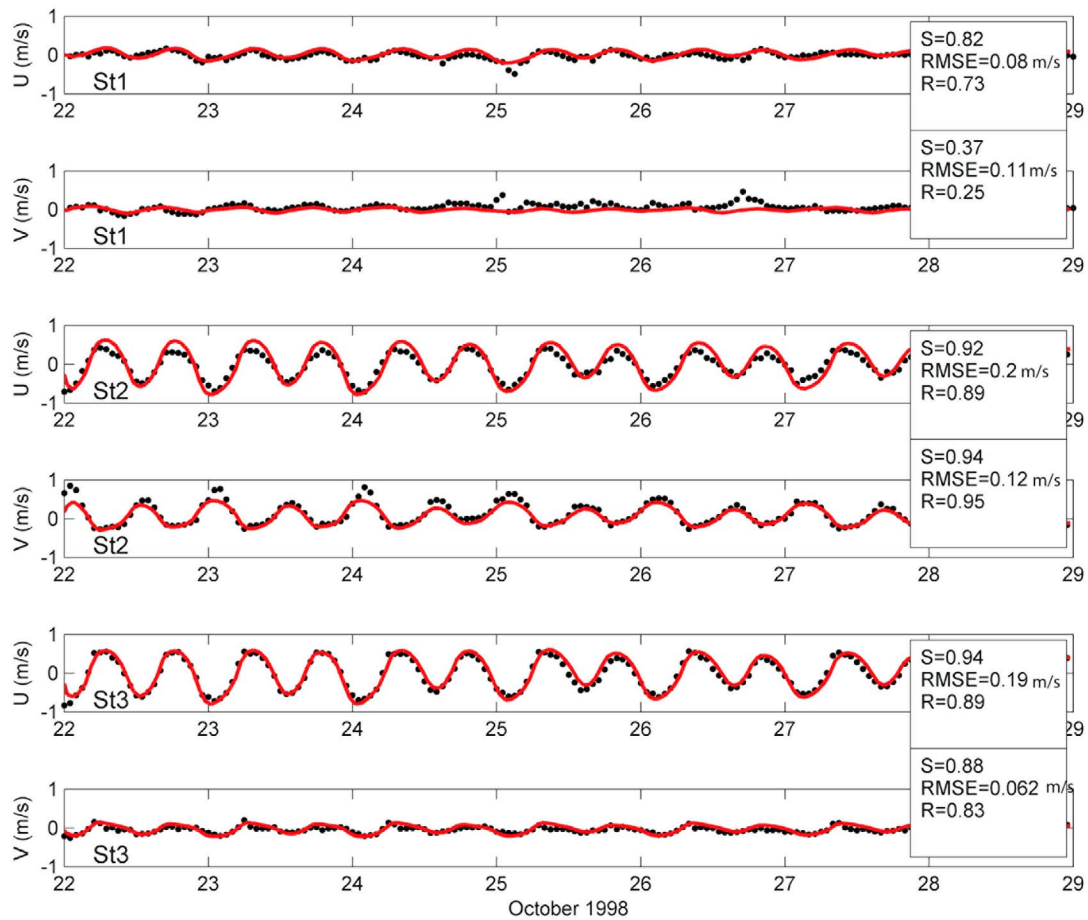
Figure 8. Time variation of (a) the sea surface elevation at four different stations and (b) barotropic currents in St1, St2, and St3. Dots represent measurements while the continuous lines correspond to the numerical simulations results (U, eastward barotropic current component; V, northward barotropic current component). Notice how in St4 the resolution of the measurements was higher than in the rest of the stations.
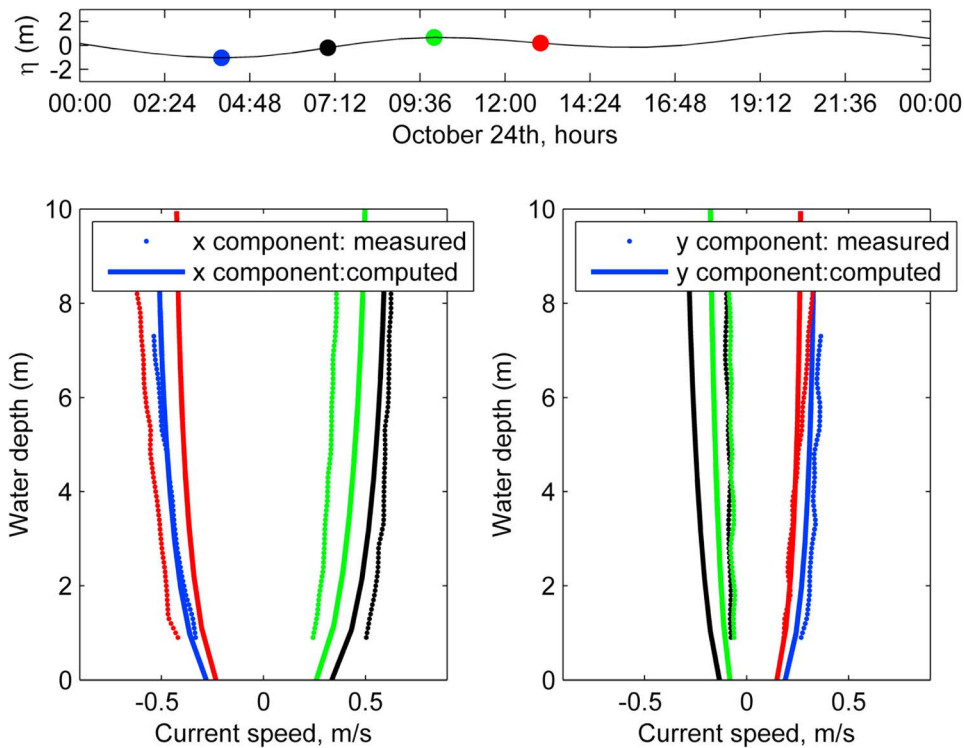
Figure 9. Current profiles measured on 24 October at St2. Dots represent measurements, while the continuous lines correspond to the numerical simulation's results.

friction. Cross-stream balances are dominated by centrifugal acceleration and pressure gradient. Near slack, balances more closely follow linear wave dynamics, with local accelerations balancing pressure gradients, and to a lesser extent Coriolis. In the case of the Willapa Inlet, without considering the effect of waves, momentum balances are similar to those observed by *Hench and Luettich* [2003]. During the ebb and flood, the momentum balance is dominated by horizontal advection, pressure gradient, and bottom friction. As an example, Figure 10 shows the leading terms on the momentum balance equation for the maximum ebb phase. During the maximum ebb, when the jet current showed its largest extension offshore, the maximum offshore-directed pressure gradients were obtained in the inlet area.

[48] Because of the inlet's complex channel system, the pressure gradient term (prsgrd) showed local variations with maximum values in the channels and in the ebb shoal's shallowest areas. The bottom stress (bstr) also showed maximum values in these locations, balancing the pressure gradient term. Horizontal advective terms (xadv and yadv) were also important in the main channels, alternating positive and negative values along the inlet area. However, the two horizontal advection terms showed opposite patterns and basically balanced each other. The local acceleration term was close to zero, indicating a little change in the flow speed. In slack water the pressure gradient between the sound and the ocean weakened. Because of the flow reduction in the inlet area, advective terms lost importance in the momentum balance while the local acceleration (accel) became more important. At this tidal phase there was a balance among local acceleration, bottom friction, and

pressure gradient. During the flood (not shown) the pressure gradient between the ocean and the sound was directed into the bay and showed maximum values in the inlet area. This term was balanced by the bottom friction. The advective terms balanced each other and showed patterns similar to those observed during the ebb, with the difference that during the ebb these terms were important offshore of the inlet, all along the extension of the jet current.

[49] When wave forces were modeled (R1), the momentum balance during the maximum ebb in the inlet area changed considerably (Figure 11). Wave-breaking-induced accelerations played an important role in the momentum balance when considering waves. Unlike advective terms, the total pressure gradient and bottom friction greatly changed in response to waves. In all tidal phases, the offshore-directed pressure gradient was enhanced offshore of the ebb shoal and all along the wave-breaking zone, partially balancing the wave-breaking-induced accelerations.

[50] In the ebb shoal area the bottom friction changed in different ways in response to a wave's effects. During the

Table 1. Coherence Between Model and Measurements[a]

Model	RMSE (m/s)	R	Skill, S
P1, x St2 (blue)	0.019	0.99	0.96
P1, y St2 (blue)	0.03	0.97	0.72
P2, x St2 (black)	0.06	0.98	0.70
P2, y St2 (black)	0.15	0.81	0.27
P3, x St2 (green)	0.11	0.99	0.48
P3, y St2 (green)	0.07	0.87	0.33
P4, x St2 (red)	0.16	0.98	0.34
P4, y St2 (red)	0.026	0.96	0.83

[a]Current profiles in St2 shown in Figure 9.

Table 2. Summary of the Model Runs

Run	ELV	CUR	VF-BH	BRK	ROL	KAW	TKE	Comments
R0	✓	✓	✗	✗	✗	✗	✗	Tidal propagation, no wave effects
R1	✓	✓	✓	✓	✓	✓	✓	Fully coupled baseline (section 5)
R2	✓	✗	✓	✓	✓	✓	✓	No feedback of currents on waves
R3	✗	✗	✓	✓	✓	✓	✓	No feedback of currents and elevations on waves
R4	✓	✓	✓	✓	✓	✗	✓	No wave-induced bottom roughness

ebb, because of the enhancement of the apparent bed roughness by waves, the bottom friction increased. During the flood the bottom friction showed maximum values offshore of the ebb shoal. Only these two nonconservative wave forces, the wave-enhanced bottom stress and the wave-breaking-induced accelerations, had a significant influence on the horizontal momentum balance. The vortex force and the rest of the wave force terms were of second order and did not create significant changes in any of the analyzed tidal phases. It is noteworthy that the TKE term might be more important when processes in the surface mixed layer are being examined or when the potential for stratification exists, and this term might be important if nearshore processes were being examined more closely. However, in the scale of analysis of the present study, the effect of those terms is at least one order of magnitude smaller than the effect of wave-breaking-induced accelerations and the apparent bed roughness enhancement. From the present analysis it can be concluded that during this

storm, tidal inlet dynamics were controlled both by surf zone processes and tidal propagation, and none of these dynamics can be neglected.
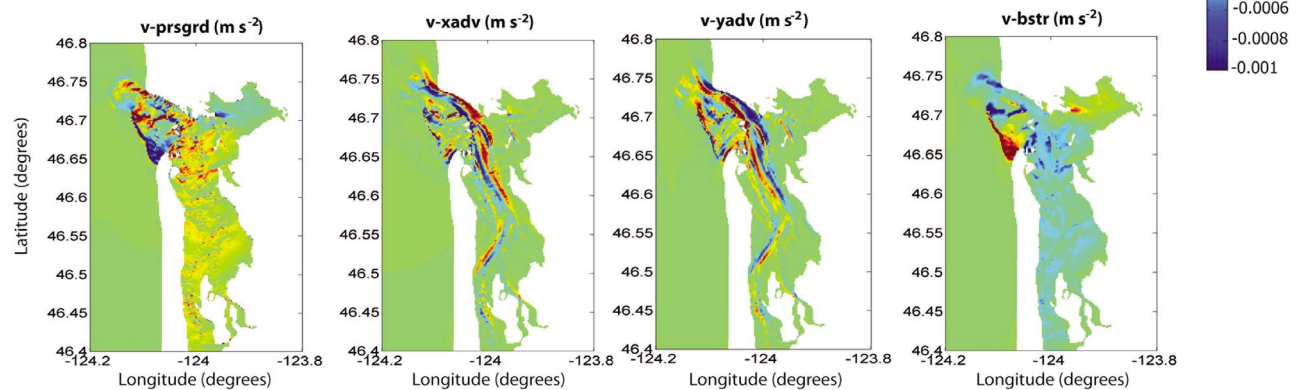
[51] Figure 12 shows the different pressure gradient terms in the x momentum balance equation during the maximum ebb phase of 25 October obtained in run R1. In all the analyzed tidal phases, the total pressure gradient term was dominated by the current contribution (P^c) and the quasi-static response (P^{qs}) in the exterior part of the inlet and in the surf zone. In general, the Bernoulli Head term (P^{BH}) and the surface pressure boundary correction (P^{pc}) were not as important as P^c and P^{qs}. The main contribution of the Bernoulli Head term (P^{BH}) was located over the shallowest parts of the ebb shoal because of the high shear of the flow velocities in this region. The pressure correction term was more important in the inner part of the inlet.

[52] In order to analyze how the changes of wave forces affected sea surface elevations and barotropic currents, we compared results obtained in runs R0, R1, and R4. With

Figure 10. Leading terms of the momentum balance equation for the maximum ebb phase on 25 October, run R0. (a) The x momentum balance terms. (b) The y momentum balance terms.
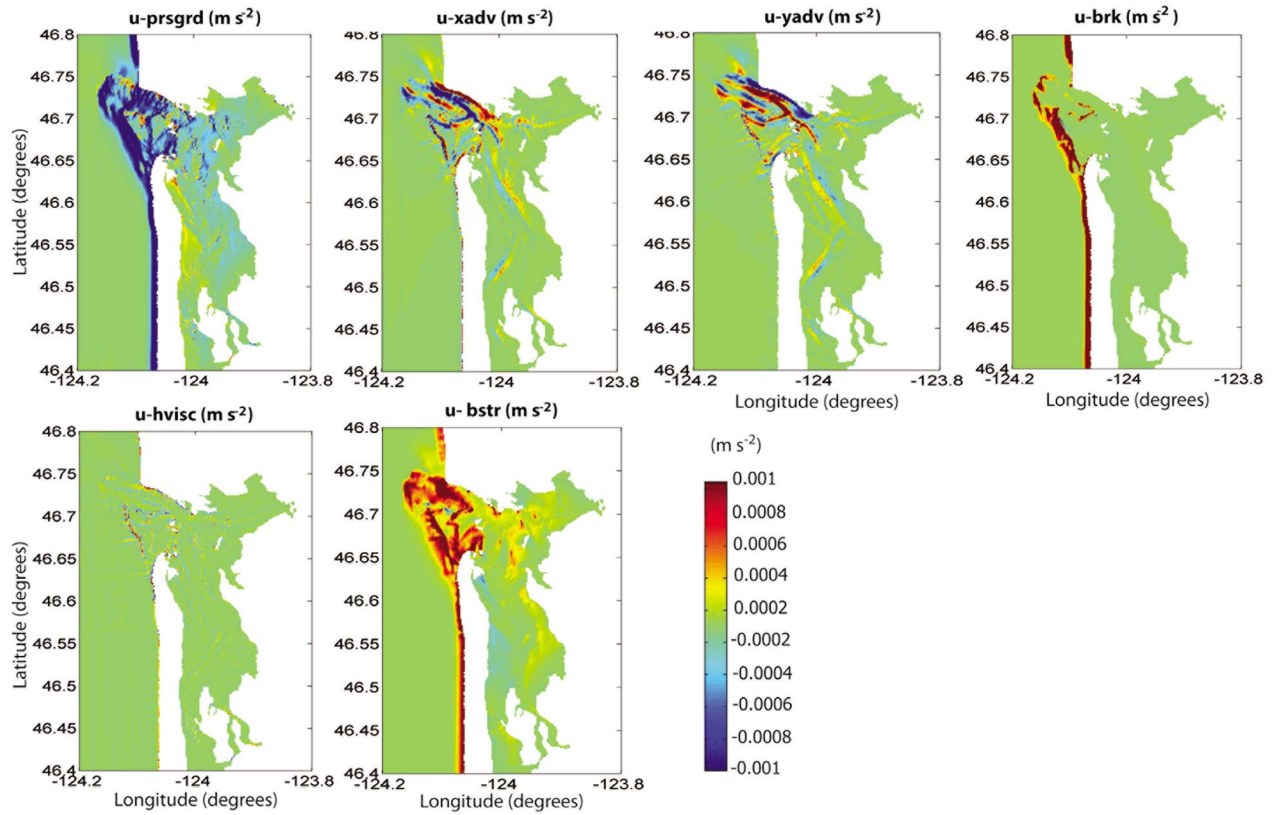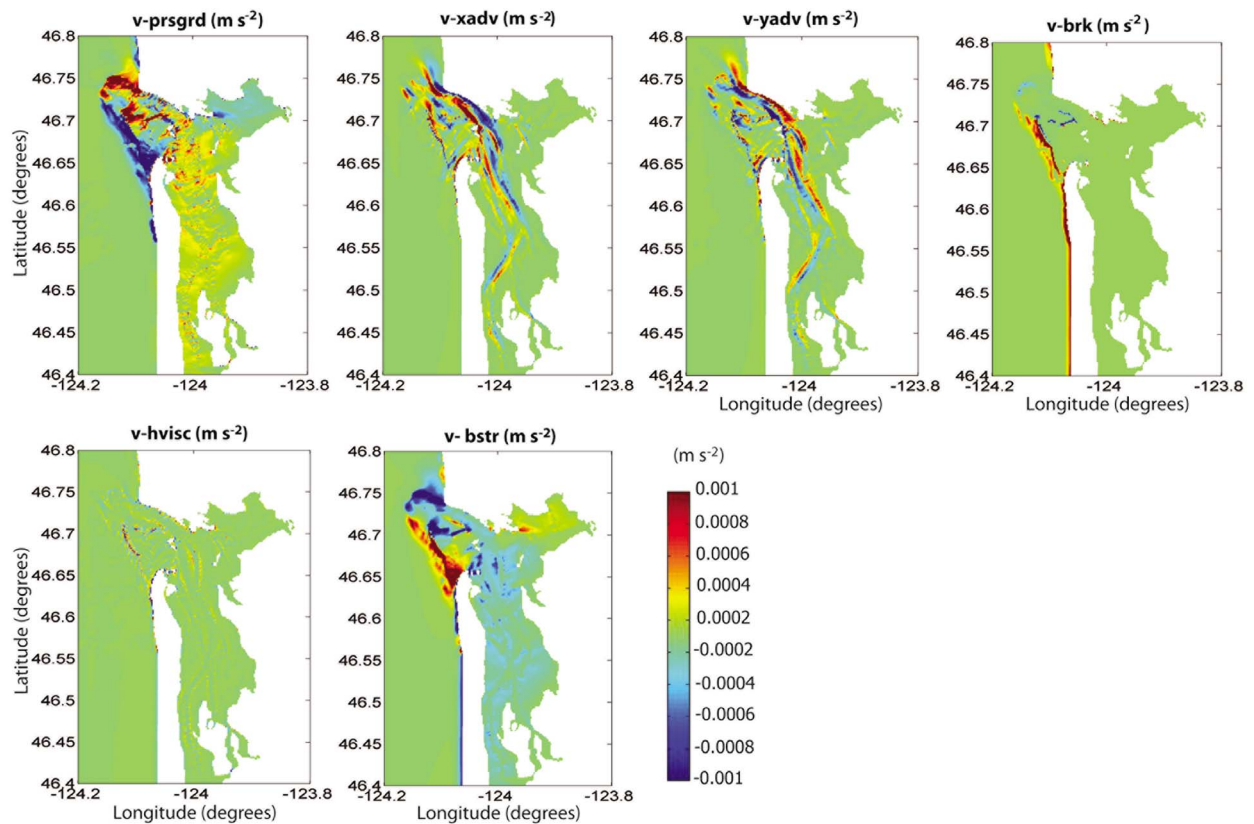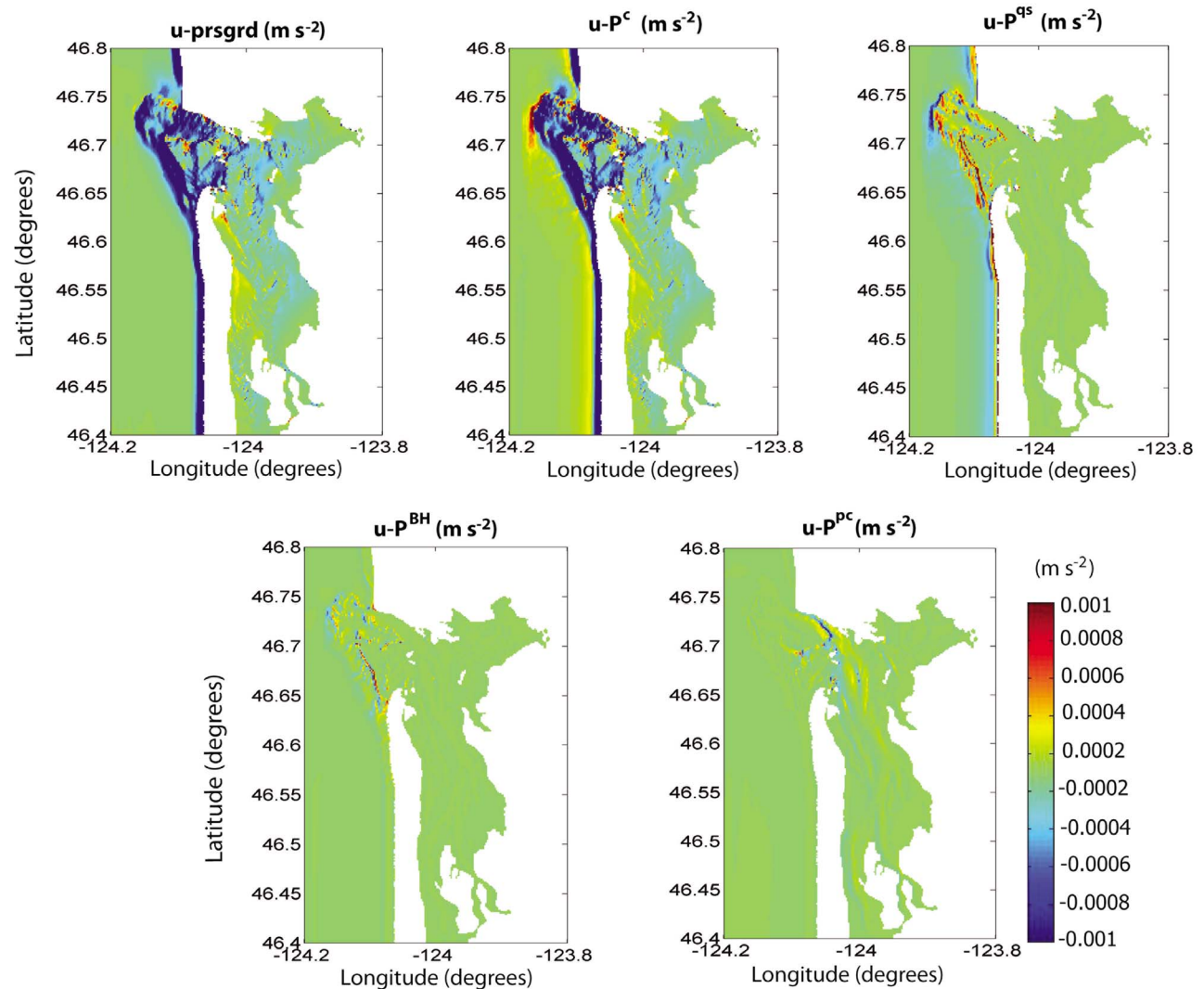
a) x momentum balance terms

b) y momentum balance terms

Figure 11. Leading terms of the momentum balance equation for the maximum ebb phase on 25 October, run R1. (a) The *x* momentum balance terms. (b) The *y* momentum balance terms.

x momentum pressure gradient terms

Figure 12. Terms contributing to the total pressure gradient term in the *x* momentum balance equation during the maximum ebb phase on 25 October, run R1.

regard to sea surface elevations, we could identify that outside the estuary, waves created a setdown before the breaking point and a setup in the surf zone area. This setdown-setup system was visible in the exterior part of the Willapa Bay spit and also in the inlet area. The wave-induced setup affected the inlet zone as well as had a direct effect all over the estuary. During the storm on 24 October, a wave-induced mean sea level rise inside the estuary reached 0.25 m in the southernmost corner. Figure 13 depicts the time series of the modeled wave-induced setup in the stations (St1, St2, St3, St4, and St5). The wave-induced setup was obtained by the differences in the sea surface elevations between runs R0 and R1. Figure 13 (top) shows the time evolution of the modeled significant wave height just offshore of the ebb shoal. Figure 13 (bottom) shows the wave-induced sea level variations in the different stations. Results showed that the main effect of waves was a setup inside the estuary that increases with the offshore energy. *Guza and Thorton* [1981], *Hanslow and Nielsen* [1992], *Hanslow et al.* [1996], *Dunn*

et al. [2000], *Oshiyama et al.* [2001], *Tanaka et al.* [2000, 2003], *Nguyen et al.* [2007], and *Malhadas et al.* [2009] have identified a wave-induced setup in inlets, river entrances, and lagoons. *Malhadas et al.* [2009] stated that the wave-induced setup in estuaries depends not only on the offshore significant wave height but also on the inlet morphology. They developed an idealized inlet-lagoon model that considered the effects of the wave-induced vertically integrated radiation stress gradients. They observed that the wave setup height inside the lagoon depends not only on the offshore wave height but also on tidal inlet morphology, mainly depth and length. They concluded that the deeper and shorter the morphology, the more the wave setup is reduced, as shown by the numerical solution of the simple idealized model.

[53] Corroborating these previous studies about wave-induced setup in inlets, in the case of Willapa Bay the highest setup coincided with the moment of the most energetic waves offshore, reaching values of about 0.25 m
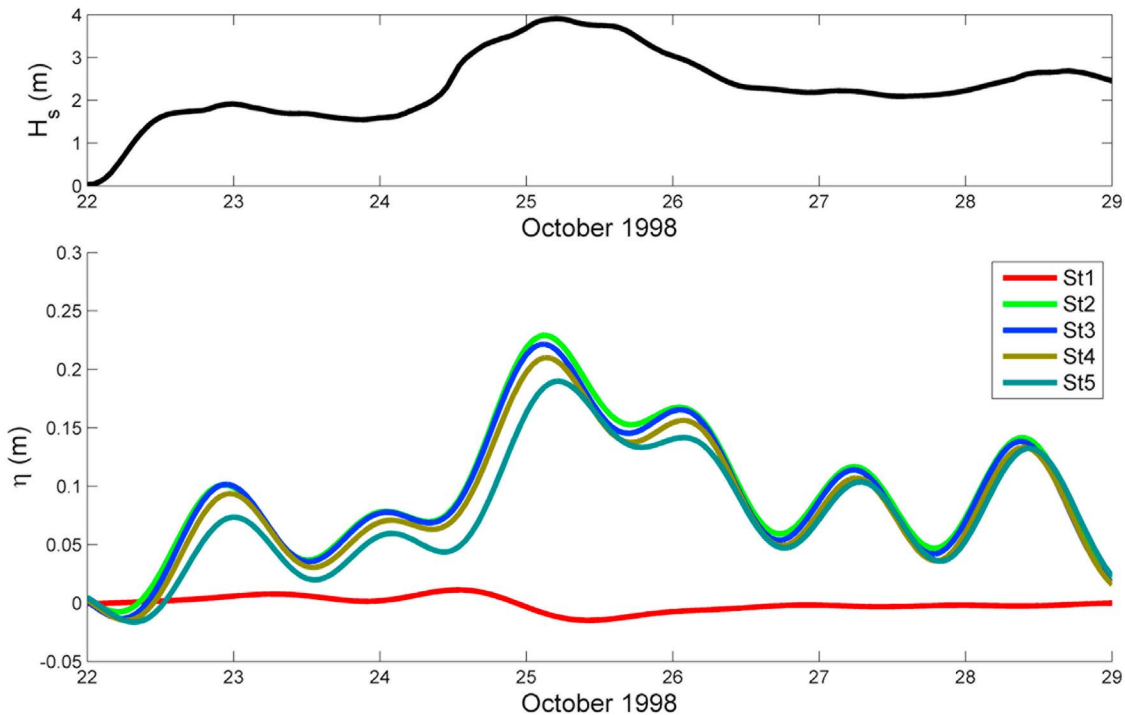
Figure 13. Time series of the wave-induced setup in the stations (St1, St2, St3, St4, and St5). Wave-induced setup was obtained by the difference on the sea surface elevations between runs R0 and R1.

inside the estuary. Taking into account that the basin area is approximately 260 km^2, the amount of water added to the estuary by offshore waves was 65×10^6 m^3 (11.8% of the tidal prism during the analyzed storm). The main forcing mechanism of the wave-induced setup was the wave-breaking acceleration. When waves break over the shoal, the wave-breaking-induced acceleration is directed toward the inlet mouth and pumps water into the estuary. The intensity of this force depends on the amount of energy dissipated during the breaking processes. Since wave breaking in the inlet zone depends on the water depth, the intensity of the wave-breaking-induced acceleration is tidally modulated, as is the wave-induced setup. During these numerical simulations the peak storm wave height at station St1 was underestimated, and therefore the wave dissipation produced a smaller setup than in reality. Observations (at St4) showed that this setup was about 0.3 m during the storm's peak.

[54] The apparent bed roughness enhancement was the second most relevant process with regard to wave-induced sea level variations, but was of second order. Its effect was not an increase of the mean water level, but rather a reduction of the amplitude of the tidal astronomic components and also a change of phase of the tide. At each point a harmonic analysis was performed using the T_Tide program [Pawlowicz et al., 2002] to provide the amplitude and phases of the main harmonic component (M2) and its first superhamonic (M4) (see Table 3).

[55] These changes of the amplitude and phases are indicative of the total dissipation and tidal deformation induced by the increase of the bottom friction because of waves. The apparent bed roughness reduced the amplitude of the first harmonic of approximately 6 cm. The changes in the phase were also important, with values of about 5°. The

amplitude of the first superharmonic was small in general, which means that the tidal deformation was not pronounced in the estuary. Its amplitude increased toward the estuary head and increased when the effect of waves was introduced. The apparent bed roughness generated a small increase of the amplitude of this first superharmonic, with the most relevant effect being the first harmonic dissipation and consequently a reduction of the tidal prism of approximately 11%.

[56] In respect to the currents in the inlet-estuary system, the most important changes when including the effect of wave-current interaction were created by the wave-breaking-induced accelerations and the bottom friction. Figure 14 depicts the barotropic currents obtained on 25 October during the maximum ebb (Figure 14a) and during maximum flood (Figure 14b).

[57] Figure 14 (left) shows the currents obtained in run R0, Figure 14 (middle) shows the fully coupled currents, and Figure 14 (right) shows the differences. During the ebb, wave-generated currents greatly affected the circulation in

Table 3. Harmonic Analysis Results for Runs R0 and R1

| Station	Run	M2 Amplitude (m)	M2 Phase (deg)	M4 Amplitude (m)	M4 Phase (deg)
St1	R1	0.81	197.5	0.0009	243.67
	R4	0.81	197.5	0.0003	218.72
St2	R1	0.67	214.28	0.025	355.49
	R4	0.72	210.83	0.023	345.28
St3	R1	0.65	222.16	0.018	12.75
	R4	0.71	217.32	0.028	109.63
St4	R1	0.64	236.04	0.017	40.22
	R4	0.71	230.68	0.008	33.04
St5	R1	0.70	255.09	0.027	90.22
	R4	0.76	248.30	0.031	80.27
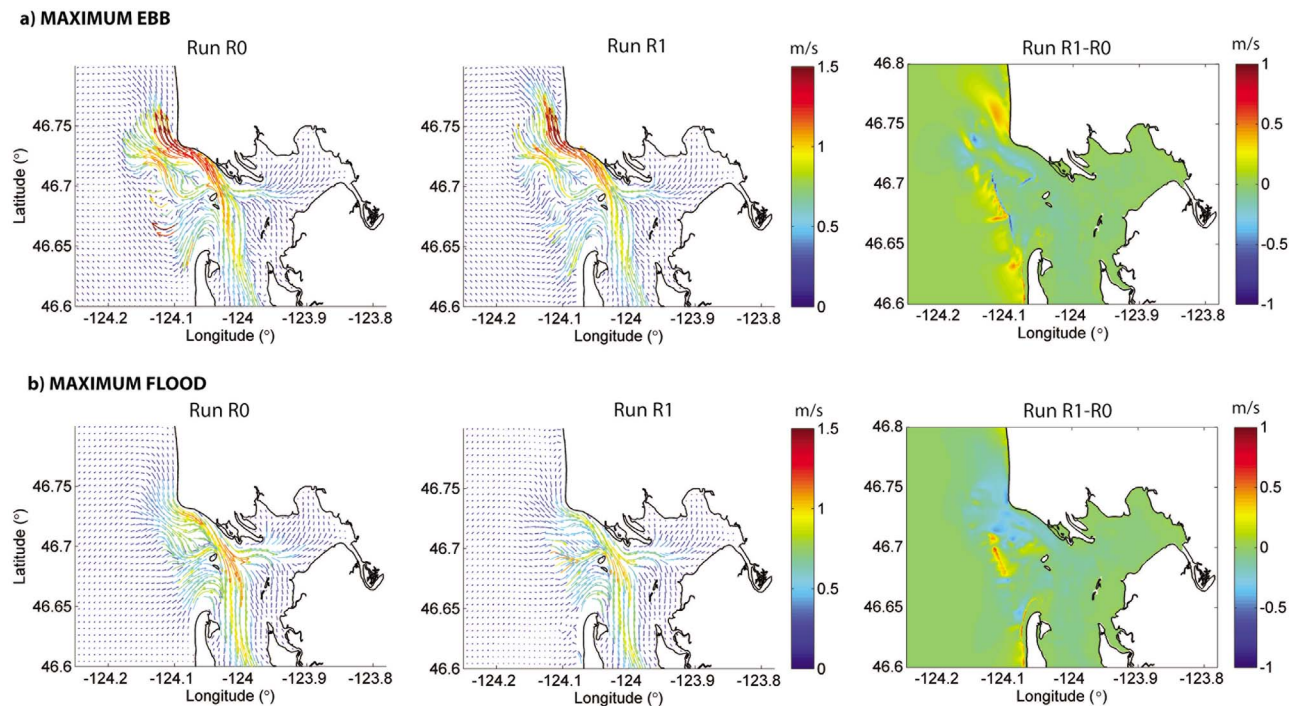
Figure 14. Barotropic currents obtained on 25 October during the maximum (a) ebb and (b) flood.

the inlet area. Wave-forced currents tended to constrict the ebb current and generated an intensification of the ebb current in the main inlet channel, making the jet narrower, more elongated, and intense. During the flood the effect was different. Locally generated wave-induced currents in the inlet tended to intensify the currents, especially in the channel located in the middle of the inlet and especially in the shallowest area of the ebb shoal. This channel was not as deep as the main channel. Comparing results from runs R0, R1, and R4, we identified that wave-breaking-induced accelerations were the main term affecting the current intensity in the inlet area, with changes up to 0.5 m/s. The next most important effect was induced by the apparent bed roughness enhancement. This term reduced the alongshore current along Long Beach by 0.1–0.15 m/s. It also reduced the magnitude of the currents in the exterior part of the ebb shoal. These reductions were compensated by intensifying the currents in some areas located in the exterior part of the inlet. In the interior part of the estuary, the increase of the apparent roughness reduced the intensity of the currents and also generated a phase change. During the storm, especially in the exterior part of the inlet and along Long Beach, the apparent bed roughness increased by two orders of magnitude because of the effect of waves. Although the roughness enhancement was not that relevant inside the estuary, the results obtained from the sea surface elevation harmonic analysis along the estuary (shown in Table 3) demonstrated that the increase achieved in the inlet zone affected the entire inner part of the estuary.

[58] The effect of wave-current interaction was not uniform in the water column, and each term involved had a different vertical influence. In the ebb shoal region, storm waves tended to increase the upper water column velocities

in the direction of the wave height gradient. The turbulent kinetic energy injection tended to diminish the current intensity and the current shear in the upper zone of the water column. During wave-breaking conditions the near-surface mixing was higher and the velocity shear was lower. These results were in agreement with previous studies [*Burchard*, 2001; *Carniel et al.*, 2009] that identified a decrease of the surface velocity when the turbulent kinetic energy injection from breaking waves was included. Figure 15 depicts the vertical distribution of the main flow acceleration terms in the x direction during the maximum ebb on 25 October. The analysis profile (see Figure 15a) extends from the offshore region (15 m water depth) to the inlet area. The water depth along this section gradually decreases from the offshore toward the inlet. At the end of the section the shallow bar represents the ebb shoal. Bayward of the ebb shoal, the increase of the water depth indicates the presence of the inlet channel. Figure 15b shows the vertical distribution of the x velocity component for the tidal propagation (Figure 15b, top) and for the fully coupled case (Figure 15b, bottom). In both cases the flow was directed offshore, as is expected during the maximum ebb. The ebb shoal region showed the maximum speeds in both cases. Notice how, without considering the effect of the waves, in the ebb shoal area an intense and rapid sea level change occurred (Figure 15b, top, near $x = -124.115$). When including the effect of the waves, although the difference between the sea surface elevation in the inlet and offshore was larger, the gradient was smoother. Water depths over the bar increased and the offshore currents reduced from 1 m/s to about 0.7 m/s because of the presence of waves. The vertical distribution of the currents did not show a strong shear in any of the analyzed tidal phases. Undertow flows were not identified in this specific storm
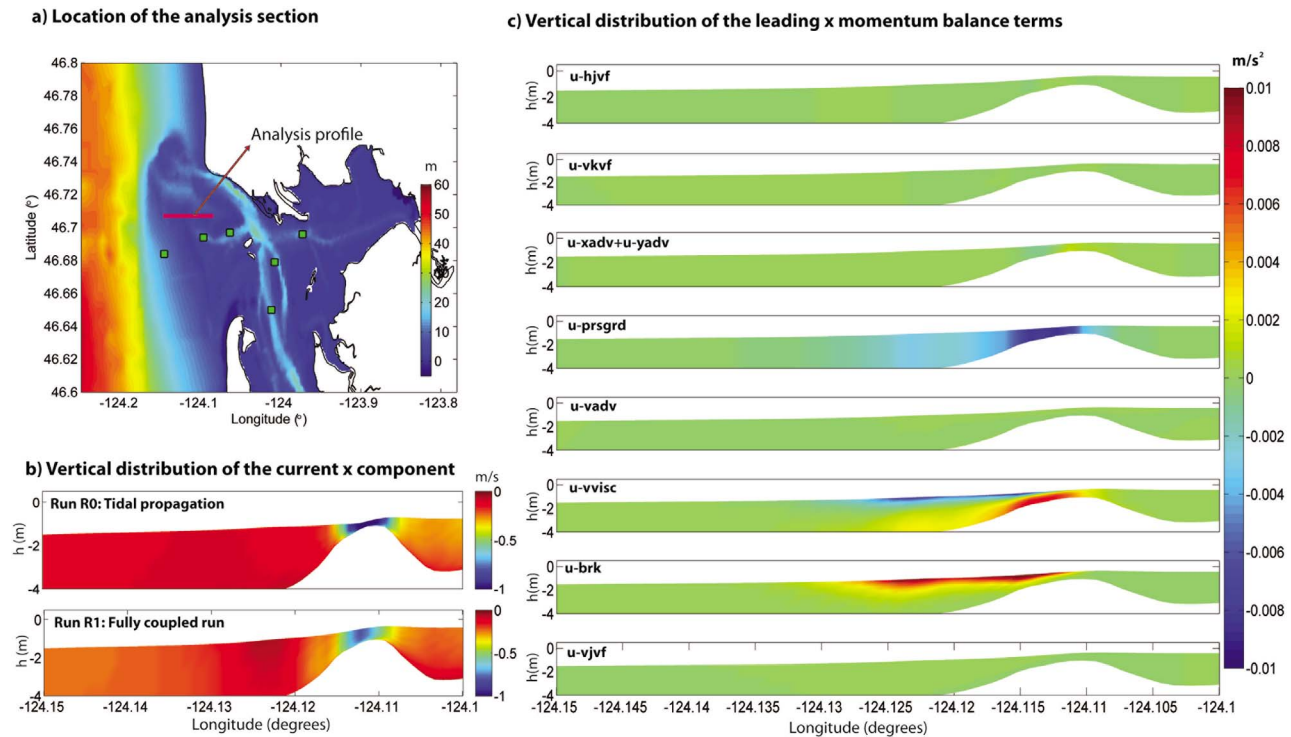
Figure 15. Vertical momentum balance analysis in the *x* coordinate during the ebb, 25 October: (a) location of the analysis section, (b) vertical sections of the *x* velocity component for runs R0 and R1 (c) leading terms off the vertical momentum balance equation for R1.

event. As shown in Figure 15c, the vertical distribution of the *x* momentum balance terms was not homogeneous through the water column. The pressure gradient as well as the horizontal advection did not show significant vertical variations. However, wave-breaking-induced acceleration was concentrated in the upper part of the water column, forcing the flow in the wave propagation direction. At the surface, breaking-acceleration-induced momentum balanced the vertical mixing and pressure gradients, while close to the bottom layers the vertical mixing and pressure gradients balanced each other. The role of vertical mixing was to redistribute the momentum concentrated at the surface to the bottom layer. Notice how over the bar the pressure gradient was partially balanced with the intense vertical mixing.

[59] The results shown in this section have demonstrated that during storm conditions the analyzed inlet's dynamics were governed by tidal and surf zone dynamics and that these dynamics were of the same order. We identified that the jet flow during the ebb veered because of the effect of the waves and that the current system in the inlet area was greatly modified essentially because of the wave-breaking-acceleration terms and because of the increase of the apparent bed roughness. Moreover, results identified that wave effects were not restricted to the inlet area and extended all over the estuary, creating an increase of the mean water level and reducing the amplitude of the main tidal components.

6.2. Effect of Tidal Currents on Waves

[60] The importance of tidal levels and current variations on wave propagation and generation was analyzed by comparing the results obtained in runs R1 (fully coupled),

R2 (coupled, only introducing sea level changes to SWAN), and R3 (coupled without considering the effect of the sea surface variations and currents on SWAN).

[61] As mentioned previously, during the analyzed storm the offshore swell from the WSW broke over the ebb shoal. The amount of energy dissipated in the shoal depended on the water depths. During high tide, the influence of swell waves extended more landward than during the low tide. Between 24 and 25 October, winds were blowing from the SSW and generated wind waves of about 0.5 m and periods of 3–4 s inside the estuary. The inlet area represented a transition zone between the sea-dominated area (the inner part of the estuary) and the swell-dominated area (the offshore region of the estuary). Results identified that the capacity of swell penetration into the inlet depended not only on water level variations that were due to tides but also on tidal currents. Moreover, the variability of the wave spectral parameters that was due to the effect of currents extended to a larger area rather than being confined to the inlet's main channels.

[62] Comparing results from runs R1 and R2, we can isolate the effect of tidal currents on the wave spectra as well as on the statistical wave parameters along the estuary. Figure 16 shows the significant wave height spatial distribution during the maximum ebb (Figure 16a) and during the maximum flood (Figure 16b) on 24 October. Figure 16 (left) represents the significant wave height when including the full effect of tides, in other words, the effect of sea level and current changes, while Figure 16 (middle) shows the significant wave height distribution obtained when only the tidal sea level changes affect the wave propagation. Figure 16 (right)
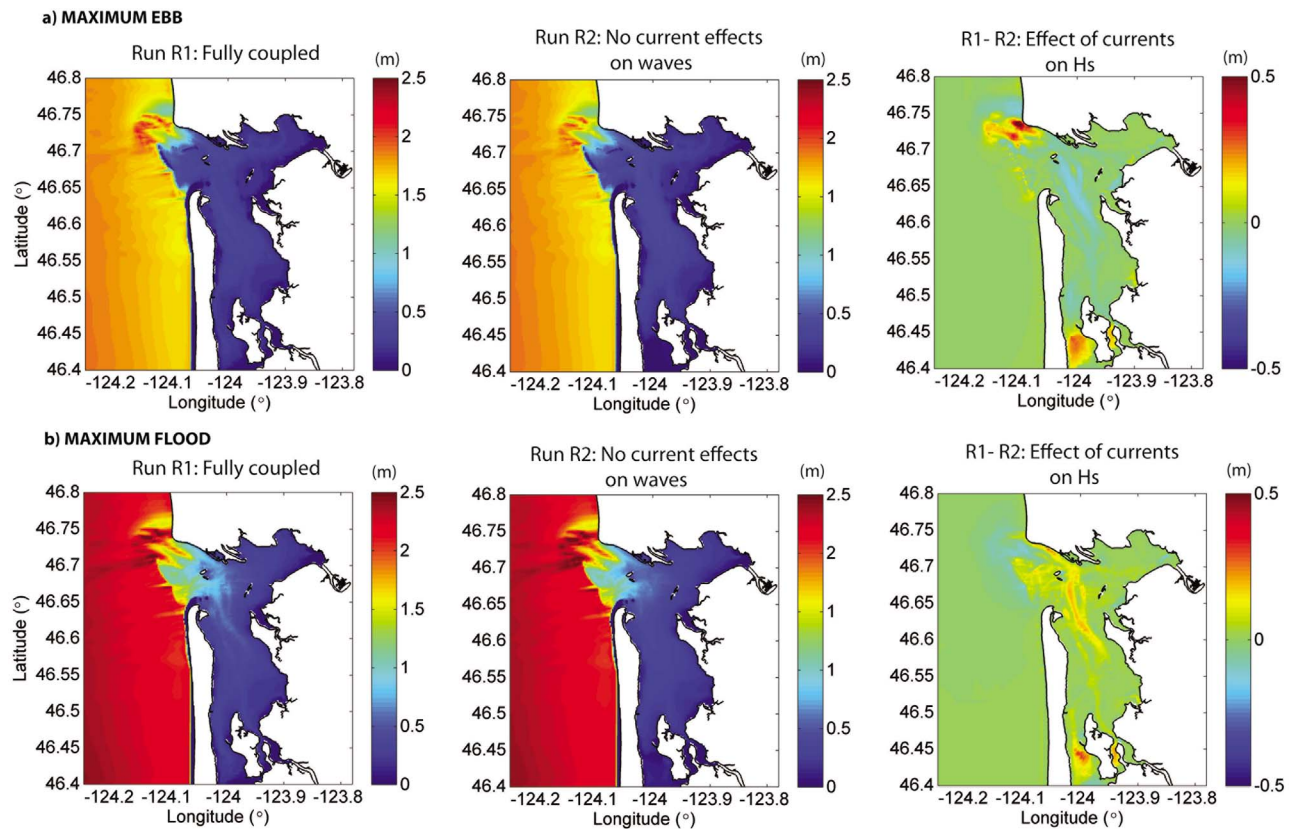
Figure 16. Significant wave heights on 24 October during maximum (a) ebb and (b) flood.

shows the differences induced by tidal currents on the significant wave height. The main differences were obtained in the exterior zone of the main channels. The ebb current jet, with maximum current speeds of about 2 m/s, refracted the waves, concentrating the wave rays and therefore focusing wave energy. Shoaling acted in a similar way to refraction, generating an increase of the wave energy and a decrease during the flood. In this zone of the inlet, the wave height increased approximately 25% during the ebb because of current-induced refraction and shoaling. However, this was not the only area in which currents created an appreciable change. All over the exterior edge of the ebb shoal current's effects were important. During the flood the significant wave height decreased in the exterior part of the ebb shoal. However, flood currents transported the offshore wave energy farther upstream, generating an increase of the swell wave energy in the inner part of the inlet.

[63] It is noteworthy that inside the estuary, along the main channel, during the flood the wave height increased because of the presence of flood currents. In this area the wave height associated with locally generated sea was small, approximately 0.5 m, and increased by about 25%. Inside the estuary, opposing currents had two different effects on sea waves. The first affected the wave generation process. Wind opposing currents increased the relative wind shear stress acting over the ocean surface, so the momentum transfer from the atmosphere to the ocean became more efficient. Opposing currents also affected the wind wave propagation inside the estuary through the current-induced

refraction and shoaling, concentrating the wave energy in the main channel.

[64] Current-induced refraction can be analyzed by the difference in the peak wave direction considering and without considering the effect of the currents (Figure 17). Current and water depth spatial gradients generate changes in the wave direction. These produce convergence or divergence of the wave rays, focusing or defocusing the wave energy. During the ebb as well as during the flood, because of the intense currents in the inlet area, wave directions changed by about 20°. However, the differences created by the currents were appreciable all over the estuary and not just in the inlet area. The maximum differences were obtained in the main channels.

[65] The comparison of the absolute mean bottom period showed that opposing currents generated a reduction of approximately 1–2 s, not only in the inlet but also in the middle part of the estuary (Figure 18). In this comparison we selected the absolute mean bottom period rather than the absolute peak period because it is the one that governs the wave boundary layer behavior and therefore wave-induced sediment transport. This parameter (T_{mbot}) is defined as the ratio of the bottom excursion amplitude to the bottom orbital velocity.

[66] From the morphological point of view, the changes in this parameter are more interesting than the changes in the absolute peak period. The mean bottom absolute period in the inlet zone and in the down part of the estuary also changed in response to tidal currents. During the ebb the
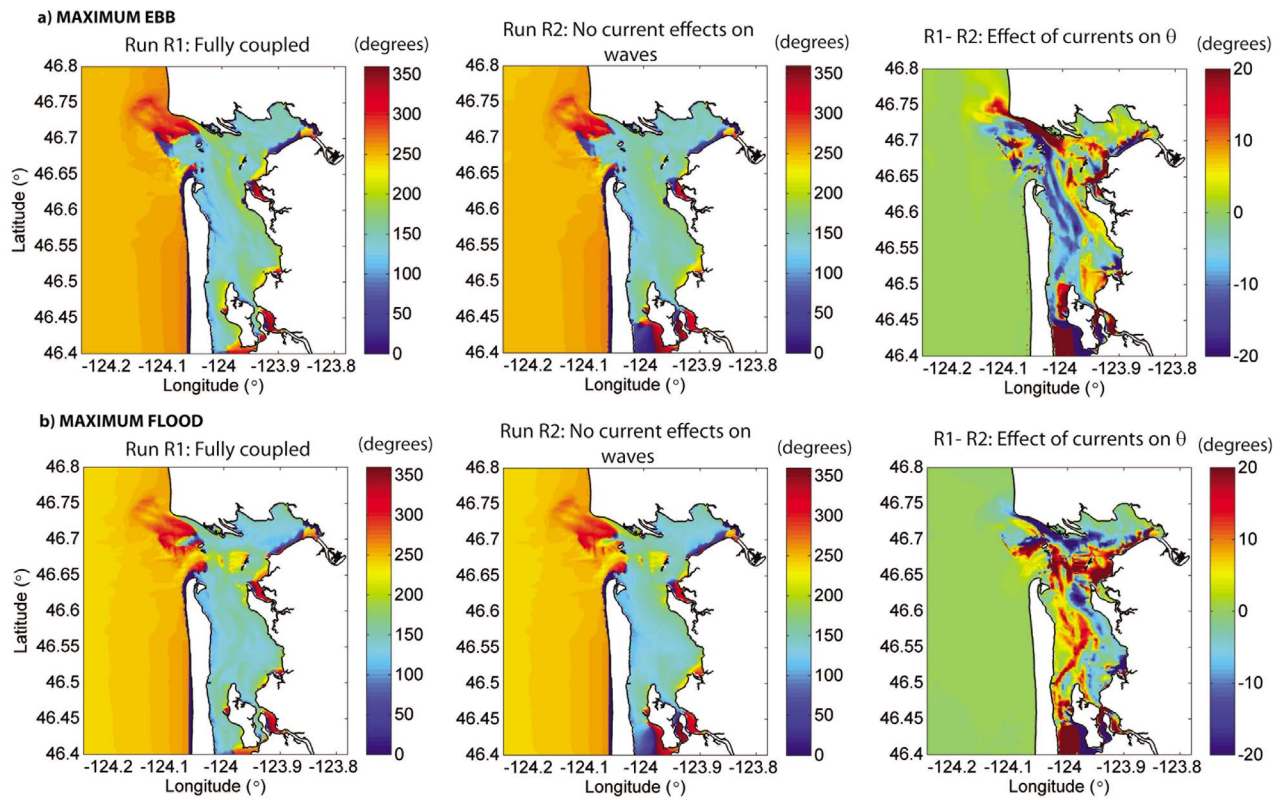
Figure 17. Wave peak directions on 24 October during maximum (a) ebb and (b) flood.
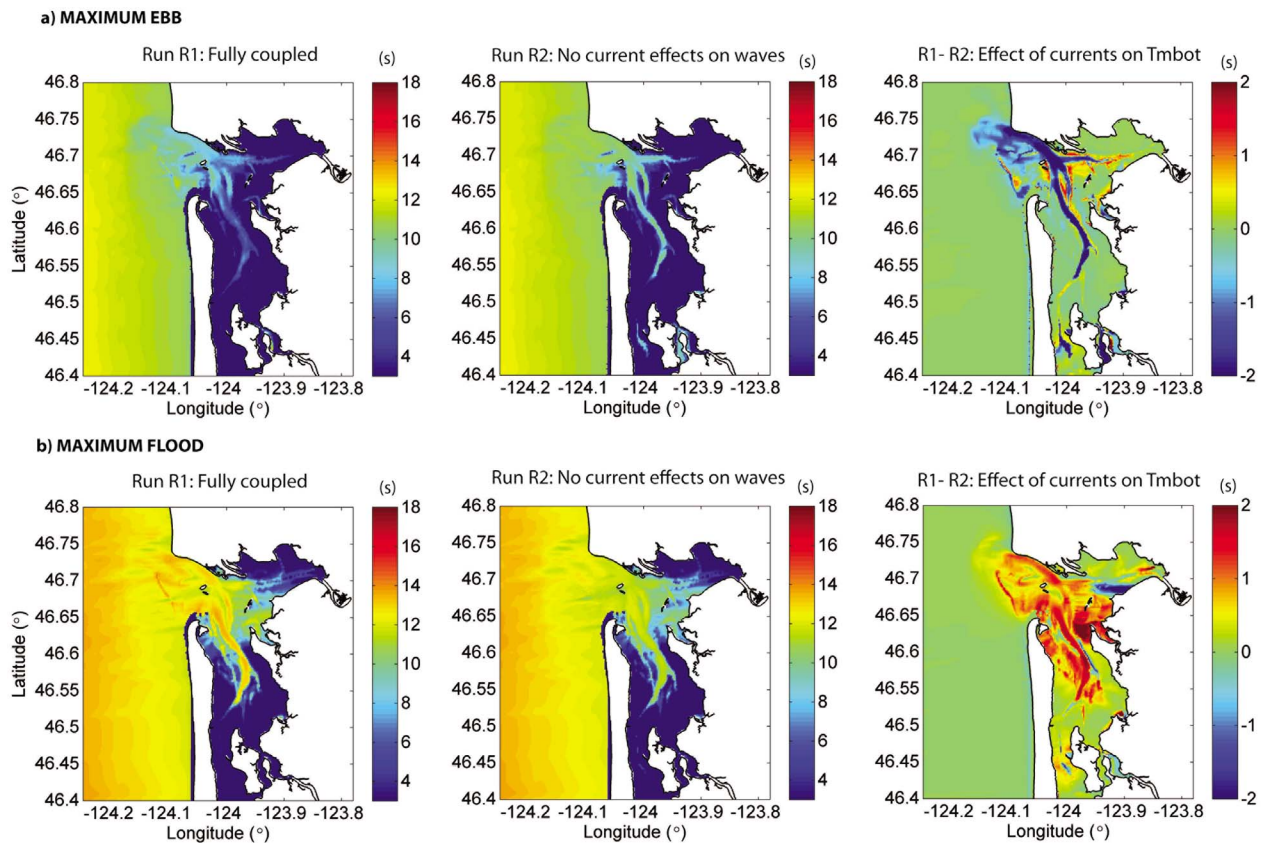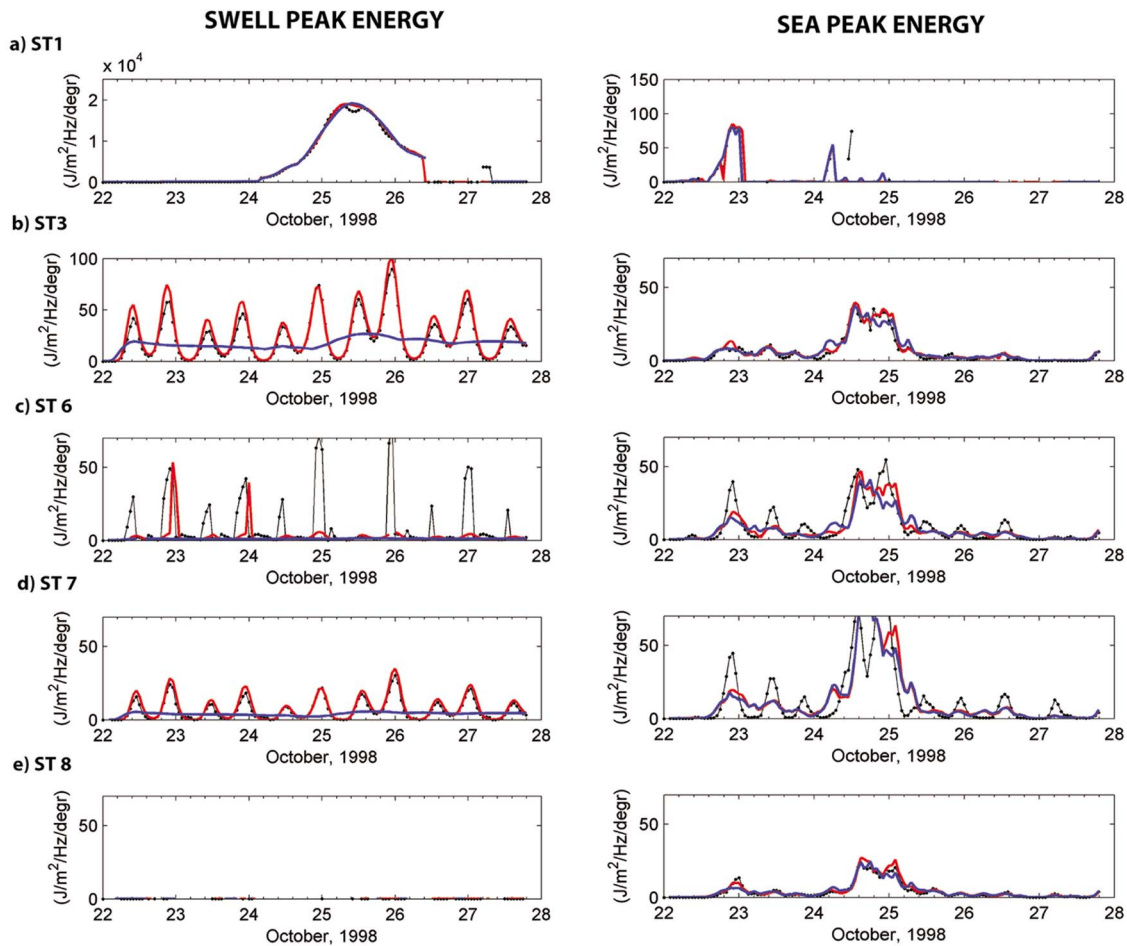

Figure 18. Absolute mean periods on 24 October during maximum (a) ebb and (b) flood.

Figure 19. Time variation of the two main spectral mode peak energies computed in runs R1 (black line), R2 (red dashed line), and R3 (blue dotted line) for different points along the estuary. Figures 19a (left)–19e (left) represent the swell peak energy (J m^{-2} Hz^{-1} deg^{-1}), and Figures 19a (right)–19e (right) represent the sea peak energy (J m^{-2} Hz^{-1} deg^{-1}).

period decreased and so did the wave height. This means that the sediment stirring capacity by sea waves in the inlet area decreased during the ebb because of the effect of the currents. On the other hand, flood currents generated an increase of the wave orbital amplitude, thereby increasing the capacity of the waves to put sediment in suspension in the inlet area. This was accompanied (not shown in the present paper) by analyzing the changes on the maximum wave-current bottom shear stresses and on wave-induced shear stresses induced by the tidal currents.

[67] Comparing the wave spectra in different points along the estuary we can analyze how currents affected the sea and swell spectral modes. Figure 19 depicts the time variations of the two main spectral modes' peak energy and absolute period computed in runs R1, R2, and R3 for different points along the estuary. The location of the analysis points was indicated in Figure 2. Station St1 was located in the swell-dominated area and tidal currents almost did not affect wave spectral characteristics. In the inlet, the wave spectra were characterized by at least two peaks, one corresponding to the offshore swell and the second to the sea generated inside the estuary. Currents affected the amount of energy contained in each mode as well as the relative

importance of swell- and sea-dominated regions. Changes in the peak directions (not shown) of both modes were also identified, and they were reflected as a tidal modulation. At station St3, the swell peak energy was greatly reduced because of the wave breaking over the shoal, and during the peak of the storm the sea energy was as high as the swell energy. Notice how currents reduced the maximum swell peak energy. Swell energy modulation basically resulted from the tidal level variations over the shoal that limited the wave energy reaching the inlet area. Currents affected absolute wave periods and were the main cause of the observed period modulation. At St6 the main energy contribution was the sea generated inside the estuary, although in some tidal phases the swell energy penetrated more upstream and the swell energy dominated over the sea.

[68] Tidal currents increased the amount of swell-dominated periods. The sea peak energy also showed a tidal modulation, and its intensity increased because of the currents. St7 and St9 were located in sea-dominated areas, and although wave periods were small the wave height was about 0.5 m. Tidal currents amplified the wave peak energy as well as wave absolute periods.

[69] The comparison of the wave spectral parameter's spatial distributions during maximum ebb and maximum flood showed that the swell-dominated area in the inlet extended more upstream during the flood than during the ebb. The inlet represented the interface between the swell-dominated region and the sea-dominated region. During the ebb and low tide the wave breaking over the shoal was stronger and currents were not able to transport the wave energy upstream, and therefore the sea-dominated area extended more seaward. Observed current-induced changes suggested that the effects of wave-current interaction were not restricted to the main channel zone and extended from the inlet area to the middle part of the estuary and more into the inner part of the estuary. The sea generated inside the estuary was affected by the tidal currents and modulations on the wave energy, wave periods, and directions were identified.

7. Summary and Conclusions

[70] The fully coupled 3-D COAWST modeling system was applied and validated at the Willapa Inlet and estuary. The model was verified with wave, water levels, and current measurements obtained in 1998 by the U.S. Army Corps of Engineers. The comparison of measured and modeled sea surface elevations and barotropic currents showed that these were correctly reproduced by the model. A reasonable agreement between observed and computed wave characteristics was obtained in the inlet area. The highest discrepancies were found at station St3. In general, it can be concluded that the coupled model correctly reproduced the main processes involved in inlet-estuarine systems.

[71] A suite of model runs was performed to isolate individual effects of various wave-current interaction processes. To analyze the effect of waves on the hydrodynamics, the vertically integrated momentum balances with and without considering the effects of waves were compared. Without considering the effect of waves, during the flood and the ebb the acceleration term was of second order while the advective terms contributed in an important way to the momentum balance. The pressure gradient and the bottom shear stress were the leading terms in the momentum balance equations. During the slack the acceleration term increased and the advective terms lost importance. These results are in agreement with the conclusions derived by *Hench and Luettich* [2003]. When including the effect of the waves, one more leading term, the wave-breaking-induced acceleration, was identified in the momentum balance. The pressure gradient terms and the bottom friction dramatically changed in order to balance this wave-induced force. In the shallowest part of the ebb shoal the TKE term also was important. In the inlet area, during the analyzed storm condition, the momentum balance shared the characteristics of a tidal-dominated environment and the surf zone, indicating the significance of these dynamics. The effects of waves on the momentum balance were manifested in current and sea elevation changes in the inlet and in the inner part of the estuary. The main process governing wave effect on currents and sea surface elevations in the inlet-estuary system was the wave-breaking-induced acceleration (which can be considered equivalent to the radiation stress gradient generation induced by breaking) in the exterior zone of the inlet. This force was responsible for the observed wave setup inside the estuary. Results showed that the setup increased with the exterior significant wave height and also showed a modulation that was due to tides. The value of the setup during the storm was about 0.25 m. With regard to the currents, the wave-generated currents changed the current patterns in the inlet zone. During the ebb and in this particular storm, the ebb current jet was narrowed and intensified in the main channel. During the flood, the wave-breaking-induced accelerations intensified the currents on those channels located in the middle of the inlet.

[72] The effect of the waves was to increase the apparent bed roughness. Although it was less important than the wave-breaking-induced acceleration, this process was also relevant. In the interior zone of the estuary the effect was a reduction of the amplitude of the main astronomic tidal components, as well as a phase change. As a consequence, a reduction of the tidal prism on about 11% was produced. This term also created a reduction of the current intensities in the surf zone (along Long Beach).

[73] In general, the effect of the turbulent kinetic energy generation during the wave breaking was one order of magnitude smaller than those changes generated by the increase of the apparent bed roughness. However, this was not the case over the ebb shoal. In this area the turbulent kinetic energy injection was important, and its effect was an increase of the mixing in the upper part of the water column, reducing the current vertical shear. Bed return flows such as undertows were not identified.

[74] Although sea level variations had a dominant role in the inlet area, current-induced refraction was also important all over the inlet and not only in the main channel. Waves propagating from offshore broke over the ebb shoal so that inside the inlet the significant wave height was depth limited and therefore, tidally modulated. However, current-induced refraction and shoaling generated peak direction changes of about 20° in many places along the inlet. Current-induced modifications on the absolute wave period were more important than those induced by water level changes. During a tidal cycle, offshore energy penetration into the inlet was modified such that during the ebb the area did not extend as landward as during the flood.

[75] Another important result derived from the analysis of the currents is that not only the waves propagating from the offshore but the waves locally generated by the wind inside the estuary were affected by the current. These were refracted and focused toward the areas of maximum currents (main channels) during the flood; the reverse occurred during the ebb. The present study has shown that wave-current interaction effects are not restricted to the inlet area, which extends its influence to the inner side of the estuary. These could affect the sediment transport rates and patterns also inside the estuary and therefore in the inner morphology. Results showed that wave-induced setups are relevant during storm conditions, retaining water volumes of about 65×10^6 m^3 inside the estuary (11.8% of the tidal prism during the analyzed storm). Depending on the severity and frequency of the storms, the residence times of the estuary as well as the wetting and drying periods of the intertidal areas could change, which could have a direct effect on many

parameters relevant from the ecological and biological points of view.

Appendix A

[76] F^w in equations (1) and (2) represent the nonconservative wave accelerations. In the present study the effect of the roller has not been considered, assuming that all the energy dissipated in the wave-breaking process is transferred to the mean currents and turbulence. The wave-breaking-induced acceleration enters as a body force through F^w in the current momentum equations and they are expressed as

$$F^w = \frac{\epsilon^b}{\rho_0 \sigma} \vec{k} f^b(z), \tag{A1}$$

where $f^b(z)$ is a vertical distribution function representing the vertical penetration of momentum associated with breaking waves from the surface, parameterized as by *Kumar et al.* [2011]:

$$f^b(z) = \cos h\left[\frac{2\pi}{H}(z + h)\right] \tag{A2}$$

where ϵ^b represents the energy dissipated in wave-breaking and whitecapping processes and H is the wave height.

Appendix B

[77] The model of *Madsen* [1994] solves the one-dimensional bottom boundary layer equation given by

$$\frac{\partial u}{\partial t} = -\frac{1}{\rho}\frac{\partial P}{\partial x_i} + \frac{\partial}{\partial z}\left(\nu_t \frac{\partial u}{\partial z}\right) \tag{B1}$$

where

$$P = p_c + p_w$$
$$u = u_c + u_w \tag{B2}$$

p_c is the pure current pressure, and p_w is the pressure corresponding to the oscillatory wave motion. The total velocity u is the sum of the current velocity u_c and the oscillatory velocity u_w.

[78] This model assumes an eddy viscosity profile scaled by $u_{*wc} = \sqrt{\tau_{wc}}$ in the wave boundary layer (WBL) and $u_{*c} = \sqrt{\tau_b}$ in the current boundary layer, calculated as

$$\nu_t = \begin{cases} \kappa u_{*wc} z, & z < \delta_{wbl} \\ \kappa u_{*c} z, & z > \delta_{wbl} \end{cases}, \tag{B3}$$

where δ_{wbl} is the thickness of the wave boundary layer (WBL), which scales as $\frac{\kappa u_{*wc} T}{2\pi}$; τ_{wc} represents the maximum vector sum of wave- and current-induced stress, but τ_b is influenced by the elevated eddy viscosity in the WBL and must be determined through an iterative process.

Appendix C

[79] Turbulent kinetic energy generation by wave breaking is included in the second-order turbulence closure model as a boundary condition for the transport equation of the turbulent kinetic energy and of the generic quantity ψ for the length scale. This last parameter is defined as

$$\psi = \left(c_\mu^o\right)^p k^m l^n, \tag{C1}$$

where k is the turbulent kinetic energy, c_μ^0 is a numerical constant dependent on the shear and stratification, and l represents the turbulent length scale. The parameters m, n, and p are specified to adequate ψ to a turbulent quantity.

[80] The transport equation for the turbulent kinetic energy is given by the following equation [*Rodi*, 1987]:

$$\frac{Dk}{Dt} = \frac{\partial}{\partial z}\left(\frac{\nu_t}{\sigma_k}\frac{\partial k}{\partial z}\right) + P + B - \varepsilon, \tag{C2}$$

where

$$P = \nu_t\left[\left(\frac{\partial u}{\partial z}\right)^2 + \left(\frac{\partial v}{\partial z}\right)^2\right] \tag{C3}$$

$$B = \left(\beta g \overline{w'\theta'} + \beta_s g \overline{w'\theta'}\right) \tag{C4}$$

P represents the production that is due to shear, B is the production or destruction by buoyancy, β and β_s are the thermal and haline concentration coefficients, respectively, σ_k is the constant turbulent Schmidt number for k, and ε accounts for the turbulent kinetic energy dissipation.

[81] The generation of k is introduced imposing the following flux boundary condition [*Feddersen and Trowbridge*, 2005]:

$$\left(\frac{\nu_t}{\sigma_k}\frac{\partial k}{\partial z}\right)\bigg|_s = \alpha \overline{\varepsilon_w}, \tag{C5}$$

where $\alpha = 0.25$ and $\overline{\varepsilon_w}$ represents the wave energy dissipation during the breaking process.

[82] The transport equation for the generic length scale as given by *Umlauf and Burchard* [2003] and as implemented by *Warner et al.* [2005] is

$$\frac{D\psi}{Dt} = \frac{\partial}{\partial z}\left(\frac{\nu_t}{\sigma_\psi}\frac{\partial \psi}{\partial z}\right) + \frac{\psi}{k}(c_1 P + c_3 B - c_2 \varepsilon F_{wall}) \tag{C6}$$

where c_1, c_2, and c_3 are coefficients, the parameter σ_ψ is the turbulence Schmidt number for ψ, and F_{wall} is a wall function. The boundary condition to take into account wave breaking is [*Carniel et al.*, 2009]

$$\left(\frac{\nu_t}{\sigma_\psi}\frac{\partial \psi}{\partial z}\right)\bigg|_s = -\frac{\sigma_k}{\sigma_\psi}\left(c_\mu^0\right)^p m\, k^{m-1}(\kappa(z_0 - z))^n c_w\left(u_s^*\right)^3$$
$$- \frac{\nu_t}{\sigma_\psi}\left(c_\mu^0\right)^p n k^m \kappa^n (z_0 - z)^{n-1} \tag{C7}$$

where u_s^* is the friction velocity; c_w is a parameter that depends on the sea state, with a typical value of $c_w = 100$ (without wave breaking the value is set to, $c_w = 0$ and therefore under nonbreaking wave conditions the first term on the right-hand side of equation (C7) vanishes to zero at the surface, resulting in the boundary conditions [*Warner et al.*,

2005, equation 54]; and z_0 is the surface roughness or the surface mixing length. For breaking wave conditions *Stacey* [1999] proposed the following closure model for the surface roughness:

$$z_0 = \alpha_w H_s$$
$$\text{where } \alpha_w = 0.5. \tag{C8}$$

Appendix D

[83] The coherence between the model and measurements was analyzed by the root-mean-square error (RMSE), the correlation coefficient (R), and model performance (skill, S). Considering that M_n and C_n are the measured data and the computed data, respectively, at N discrete points, the RMSE is given by

$$RMSE = \left[\frac{1}{N}\sum_{n=1}^{N}(M_n - C_n)^2\right]^{1/2}. \tag{D1}$$

[84] The correlation coefficient (R) between M_n and C_n is defined by

$$R = \frac{\frac{1}{N}\sum_{n=1}^{N}\left(M_n - \overline{M_n}\right)\left(C_n - \overline{C_n}\right)}{\sigma_C\sigma_M} \tag{D2}$$

where σ_M and σ_C are the standard deviations of the measured and computed data, respectively. The overbar represents the mean value. The correlation ranges from 0 (bad correlation) to 1 (good correlation).

[85] The model performance (skill, S) formulation proposed by *Wilmott* [1981] is given by

$$S = 1 - \frac{\sum_{n=1}^{N}|C_n - M_n|^2}{\sum_{n=1}^{N}\left(|C_n - \overline{M_n}|^2 + |M_n - \overline{M_n}|^2\right)}. \tag{D3}$$

This skill formulation ranges from 0 (bad skill) to 1 (good skill).

References

Banas, N. S., and B. M. Hickey (2005), Mapping exchange and residence time in a model of Willapa Bay, Washington, a branching, macrotidal estuary, *J. Geophys. Res.*, *110*, C11011, doi:10.1029/2005JC002950.

Bertin, X., A. B. Fortunato, and A. Oliveira (2009), A modelling-based analysis of processes driving wave-dominated inlets, *Cont. Shelf Res.*, *29*, 819–834, doi:10.1016/j.csr.2008.12.019.

Booij, N., R. C. Ris, and L. H. Holthuijsen (1999), A third-generation wave model for coastal regions, Part I, Model description and validation, *J. Geophys. Res.*, *104*(C4), 7649–7666, doi:10.1029/98JC02622.

Burchard, H. (2001), Simulating the wave-enhanced layer under breaking surface waves with two-equation turbulence models, *J. Phys. Oceanogr.*, *31*, 3133–3145, doi:10.1175/1520-0485(2001)031<3133:STWELU>2.0.CO;2.

Carniel, S., J. C. Warner, J. Chiggiato, and M. Sclavo (2009), Investigating the impact of surface wave breaking on modeling the trajectories of drifters in the northern Adriatic Sea during a wind-storm event, *Ocean Modell.*, *30*, 225–239, doi:10.1016/j.ocemod.2009.07.001.

Chassignet, E. P., H. G. Arango, D. Dietrich, T. Ezer, M. Ghil, D. B. Haidvogel, C.-C. Ma, A. Mehra, A. M. Paiva, and Z. Sirkes (2000), DAMEE-NAB: The base experiments, *Dyn. Atmos. Oceans*, *32*, 155–183, doi:10.1016/S0377-0265(00)00046-4.

Dalrymple, R. W., B. A. Zaitlin, and R. Boyd (1992), Estuarine facies models: Conceptual basis and stratigraphic implications, *J. Sediment. Petrol.*, *62*, 1130–1146.

Dunn, S. L., P. Nielsen, A. P. Madsen, and P. Evans (2000), Wave setup in rivers, in *Proceedings of the International Conference on Coastal Engineering*, pp. 3432–3445, Am. Soc. Civ. Eng., Reston, Va.

Emmett, R., R. Llanso, J. Newton, R. Thom, M. Hornberger, C. Morgan, C. Levings, A. Copping, and P. Fishman (2000), Geographic signatures of North American west coast estuaries, *Estuaries*, *23*, 765–792, doi:10.2307/1352998.

Feddersen, F., and J. H. Trowbridge (2005), The effect of breaking on surf-zone turbulence and alongshore currents: A modeling study, *J. Phys. Oceanogr.*, *35*, 2187–2203, doi:10.1175/JPO2800.1.

Flather, R. A. (1976), A tidal model of the north-west European continental shelf, *Mem. Soc. R. Sci. Liege*, *6*(10), 141–164.

Gonzales, F. I., E. D. Cokelet, J. F. R. Gower, and M. R. Mulhern (1985), SLAR and in-situ observations of wave-current interaction on the Columbia River Bar, in *The Ocean Surface*, edited by Y. Toba and H. Mitsuyasu, pp. 303–310, D. Reidel, New York.

Guza, R. T., and E. B. Thorton (1981), Wave set-up on a natural beach, *J. Geophys. Res.*, *86*(C5), 4133–4137, doi:10.1029/JC086iC05p04133.

Haas, K. A., and J. C. Warner (2009), Comparing a quasi-3D to a full 3D nearshore circulation model: SHORECIRC and ROMS, *Ocean Modell.*, *26*(1–2), 91–103.

Haas, K. A., I. A. Svendsen, and M. C. Haller (1998), Numerical modeling of nearshore circulation on barred beach with rip channels, in *Proceedings of the 26th International Conference on Coastal Engineering*, pp. 801–814, Am. Soc. Civ. Eng., Reston, Va.

Haidvogel, D. B., H. G. Arango, K. Hedstrom, A. Beckmann, P. Malanotte-Rizzoli, and A. F. Shchepetkin (2000), Model evaluation experiments in the North Atlantic Basin: Simulations in nonlinear terrain-following coordinates, *Dyn. Atmos. Oceans*, *32*, 239–281, doi:10.1016/S0377-0265(00)00049-X.

Haidvogel, D. B., et al. (2008), Regional ocean forecasting in terrain-following coordinates: Model formulation and skill assessment, *J. Comput. Phys.*, *227*(7), 3595–3624.

Hanslow, D. J., and P. Nielsen (1992), Wave setup on beaches and in river entrances, in *Proceedings of the 23rd International Conference on Coastal Engineering*, pp. 240–252, Am. Soc. Civ. Eng., Reston, Va.

Hanslow, D. J., P. Nielsen, and K. Hibbert (1996), Wave setup in river entrances, in *Proceedings of the 25th International Conference on Coastal Engineering*, pp. 2244–2257, Am. Soc. Civ. Eng., Reston, Va.

Hedgpeth, J. W., and S. Obrebski (1981), *Willapa Bay: A Historical Perspective and a Rationale for Research*, Coastal Ecosystems Project, Office of Biological Services, Fish and Wildlife Services, U.S. Dept. of the Interior, Washington, D.C.

Hench, J. L., and A. Luettich Jr. (2003), Transient tidal circulation and momentum balances at a shallow inlet, *J. Phys. Oceanogr.*, *33*, 913–932, doi:10.1175/1520-0485(2003)33<913:TTCAMB>2.0.CO;2.

Jarret, J. T. (1976), Tidal prism-inlet area relationships, *GITI Rep. 3*, Waterw. Exp. Sta., U.S. Army Corps of Eng. Res. and Dev. Cent., Vicksburg, Miss.

Kang, K., and D. Di Iorio (2006), Depth-and current-induced effects on wave propagation into the Altamaha River Estuary, Georgia, *Estuarine Coastal Shelf Sci.*, *66*, 395–408, doi:10.1016/j.ecss.2005.09.008.

Kirby, J. T., and T.-M. Chen (1989), Surface waves on vertically sheared flows: Approximate dispersion relations, *J. Geophys. Res.*, *94*(C1), 1013–1027, doi:10.1029/JC094iC01p01013.

Komen, G. J., S. Hasselmann, and K. Hasselmann (1984), On the existence of a fully developed wind-sea spectrum, *J. Phys. Oceanogr.*, *14*, 1271–1285, doi:10.1175/1520-0485(1984)014<1271:OTEOAF>2.0.CO;2.

Kraus, N. C. (2000a), Study of navigation channel feasibility, Willapa Bay, Washington, *Tech. Rep. RDC/CHL-00-6*, Waterw. Exp. Sta., U.S. Army Corps of Eng. Res. and Dev. Cent., Vicksburg, Miss.

Kraus, N. C. (2000b), Study of navigation channel feasibility, Willapa Bay, Washington, *Final Rep.*, U.S. Army Corps of Eng, Seattle District, Seattle, Wash.

Kumar, N., G. Voulgaris, and J. C. Warner (2011), Implementation and modification of a 3-D radiation stress formulation for nearshore applications, *Coastal Eng.*, doi:10.1016/j.coastaleng.2011.06.009.

Lane, E. M., J. M. Restrepo, and J. C. McWilliams (2007), Wave-current interaction: A comparison of radiation-stress and vortex-force representations, *J. Phys. Oceanogr.*, 37, 1122–1141, doi:10.1175/JPO3043.1.

Lesser, G. (2009), An approach to medium-term coastal morphological modeling, Ph.D. thesis, UNESCO-IHE, CRC Press, Boca Raton, Fla.

Liu, P. L. F., and A. Dalrymple (1979), Bottom frictional stresses and longshore currents due to waves with large angles of incidence, *J. Mar. Res.*, 36(2), 357–375.

Long, J. W., and H. T. Özkan-Haller (2005), Offshore controls on nearshore rip currents, *J. Geophys. Res.*, 110, C12007, doi:10.1029/2005JC003018.

Luettich, R. A., Jr., J. J. Westerink, and N. W. Scheffner (1992), ADCIRC: An advanced three-dimensional circulation model for shelves coasts and estuaries, report 1: Theory and methodology of ADCIRC-2DDI and ADCIRC-3DL, *Dredging Research Prog. Tech. Rep.DRP-92-6*, 137 pp., Waterw. Exp. Sta., U.S. Army Corps of Eng. Res. and Dev. Cent., Vicksburg, Miss.

Madsen, O. S. (1994), Spectral wave-current bottom boundary layer flows. Coastal engineering 1994, in *Proceedings of the 24th International Conference on Coastal Engineering*, pp. 384–398, Am. Soc. Civ. Eng., Reston, Va.

Malhadas, M. S., P. C. Leitao, A. Silva, and R. Neves (2009), Effect of coastal waves on sea level in Óbidos Lagoon, Portugal, *Cont. Shelf Res.*, 19(9), 1240–1250, doi:10.1016/j.csr.2009.02.007.

McWilliams, J. C., J. M. Restrepo, and E. M. Lane (2004), An asymptotic theory for interaction of waves and currents in coastal waters, *J. Fluid Mech.*, 511, 135–178, doi:10.1017/S0022112004009358.

Newberger, P. A., and J. S. Allen (2007), Forcing a three-dimensional, hydrostatic primitive-equation model for application in the surf zone: 1. Formulation. *J. Geophys. Res. 112*, C08018, doi:10.1029/2006JC003472.

Nguyen, X. T., H. Tanaka, and H. Nagabayashi (2007), Wave set-up at river and inlet entrances due to an extreme event, in *Proceedings of International Conference on Violent Flow 2007* [CD-ROM].

Nishimura, H. (1982), Numerical simulation of nearshore circulations, in *Proceedings of the 29th Japanese Conference on Coastal Engineering*, pp. 33–173, Jpn. Soc. Civ. Eng., Tokyo, Japan.

Oshiyama, S., H. Lee, and H. Tanaka (2001), Fluctuation characteristics of water level in medium-and-small scale river mouths [in Japanese], in *Proceedings of the 25th International Conference on Coastal Engineering*, vol. 48, pp. 411–415, Jpn. Soc. Civ. Eng., Tokyo.

Özkan-Haller, H. T., and Y. Li (2003), Effects of wave-current interaction on shear instabilities of longshore currents, *J. Geophys. Res.*, 108(C5), 3139, doi:10.1029/2001JC001287.

Park, K.-Y., and A. G. L. Borthwick (2001), Quadtree grid numerical model of nearshore wave-current interaction, *Coastal Eng.*, 42, 219–239, doi:10.1016/S0378-3839(00)00060-0.

Pawlowicz, R., B. Beardsley, and S. Lentz (2002), Classical tidal harmonic analysis including error estimates in MATLAB using T_TIDE, *Comput. Geosci.*, 28, 929–937, doi:10.1016/S0098-3004(02)00013-4.

Perlin, A., and E. Kit (2002), Apparent roughness in wave-current flow: Implication for coastal studies, *J. Hydraul. Eng.*, 128(8), 729–735, doi:10.1061/(ASCE)0733-9429(2002)128:8(729).

Putrevu, U., and I. A. Svendsen (1999), Three-dimensional dispersion of momentum in wave-induced nearshore currents, *Eur. J. Mech. B/Fluids*, 18, 409–427, doi:10.1016/S0997-7546(99)80038-7.

Reniers, A. J. H. M., E. B. Thornton, T. P. Stanton, and J. A. Roelvink (2004), Vertical flow structure during Sandy Duck: Observations and modeling, *Coastal Eng.*, 51, 237–260, doi:10.1016/j.coastaleng.2004.02.001.

Robin, N., F. Levoy, and O. Monfort (2009), Short term morphodynamics of an intertidal bar on megatidal ebb delta, *Mar. Geol.*, 260, 102–120, doi:10.1016/j.margeo.2009.02.006.

Rodi, W. (1987), Examples of calculation methods for flow and mixing in stratified fluids, *J. Geophys. Res.*, 92(C5), 5305–5328, doi:10.1029/JC092iC05p05305.

Ruessink, B. G., J. R. Miles, F. Feddersen, R. T. Guza, and S. Elgar (2001), Modeling the alongshore current on barred beaches, *J. Geophys. Res.*, 106(C10), 22,451–22,463, doi:10.1029/2000JC000766.

Sayce, C. S. (1976), The oyster industry of Willapa Bay Pages 347–356 in *Proceedings of the Symposium on Terrestrial and Aquatic Ecological Studies of the Northwest*, pp. 347–356, Eastern Washington State College Press, Cheney, Wash.

Shchepetkin, A. F., and J. C. McWilliams (2005), The regional ocean modeling system (ROMS): A split-explicit, free-surface, topography-following-coordinates ocean model, *Ocean Modell.*, 9, 347–404, doi:10.1016/j.ocemod.2004.08.002.

Smith, J. M., H. E. Bermudez, and B. A. Ebersole (2000), Modeling waves at Willapa Bay, Washington, in *Proceedings of the 27th International Conference on Coastal Engineering*, pp. 826–839, Am. Soc. Civ. Eng., Reston, Va.

Smith, S. J., and J. M. Smith (2001), Numerical modeling of waves at Ponce de Leon Inlet, Florida, *J. Waterw. Port Coastal Ocean Eng.*, 127(3), 176–184, doi:10.1061/(ASCE)0733-950X(2001)127:3(176).

Spargo, E. A., J. J. Westerink, R. A. Luettich, and D. J. Mark (2004), ENPAC 2003: A tidal constituent database for eastern North Pacific Ocean, *Tech. Rep. ERDC/CHL-TR-04-12*, Waterw. Exp. Sta., U.S. Army Corps of Eng. Res. and Dev. Cent., Vicksburg, Miss.

Stacey, M. W. (1999), Simulation of the wind-forced near-surface circulation in Knight Inlet: A parameterization of the roughness length, *J. Phys. Oceanogr.*, 29, 1363–1367, doi:10.1175/1520-0485(1999)029<1363:SOTWFN>2.0.CO;2.

Svendsen, I. A., and U. Putrevu (1994), Nearshore mixing and dispersion, *Proc. R. Soc. London, Ser. A*, 445, 1–16.

Tanaka, H., H. Nagabayashi, and K. Yamauchi (2000), Observations of wave set-up height in a river mouth, in *Proceedings of the 27th International Conference on Coastal Engineering*, pp. 3458–3471, Am. Soc. Civ. Eng., Reston, Va.

Tanaka, H., H. S. Lee, and K. Furumichi (2003), Influence of morphological change on water level rise at the Shiribetsu River mouth, *J. Hydrosci. Hydraul. Eng.*, 21(1), 71–78.

Uchiyama, Y., J. C. McWilliams, and A. F. Shchepetkin (2010), Wave-current interaction in an oceanic circulation model with a vortex force formalism: Application to the surf zone, *Ocean Modell.*, 34(1–2), 16–35.

Umlauf, L., and H. Burchard (2003), A generic length-scale equation for geophysical turbulence models, *J. Mar. Res.*, 61, 235–265, doi:10.1357/002224003322005087.

Van Dongeren, A. R., I. A. Svendsen, and U. Putrevu (1999), Quasi 3-D effects in infragravity waves, paper presented at the Coastal Engineering Conference1998, Am. Soc. of Civ. Eng., Reston, Va.

Warner, J. C., C. R. Sherwood, H. G. Arango, and R. P. Signell (2005), Performance of four turbulence closure models implemented using a generic length scale method, *Ocean Modell.*, 8, 81–113, doi:10.1016/j.ocemod.2003.12.003.

Warner, J. C., C. R. Sherwood, R. P. Signell, C. K. Harris, and H. G. Arango (2008), Development of a three-dimensional, regional, coupled wave, current, and sediment-transport model, *Comput. Geosci.*, 34(10), 1284–1306, doi:10.1016/j.cageo.2008.02.012.

Warner, J. C., B. Armstrong, R. He, and J. Zambon (2010), Development of a Coupled Ocean-Atmosphere-Wave-Sediment Transport (COAWST) modeling system, *Ocean Modell.*, 35, 230–244, doi:10.1016/j.ocemod.2010.07.010.

Weir, B., Y. Uchiyama, E. M. Lane, J. M. Restrepo, and J. C. McWilliams (2011), A Vortex-Force analysis of the interaction of rip currents and surface gravity waves, *J. Geophys. Res.*, 116, C05001, doi:10.1029/2010JC006232.

Wilmott, C. J. (1981), On validation of models, *Phys. Geogr.*, 2, 184–194.

N. Kumar, Department of Earth and Ocean Sciences, University of South Carolina, Columbia, SC 29208, USA.

M. Olabarrieta and J. C. Warner, Woods Hole Coastal and Marine Science Center, U.S. Geological Survey, 384 Woods Hole Rd., Woods Hole, MA 02543, USA. (molabarrieta@usgs.gov)